Analytical Nonlinear *m-θ* Curves for Monopiles in Clay

Abigail H. Bateman[1]; Jamie J. Crispin, Ph.D.[2]; and George E. Mylonakis, Ph.D., P.E., M.ASCE[3]

Abstract: Dependable predictions of monopile foundation response to lateral loads are crucial to the efficient design of offshore wind turbine foundations. For squat monopile foundations, it is important to incorporate the distributed nonlinear moment-rotation response with depth, known as *m-θ* curves, in addition to traditional *p-y* curves and lumped force-displacement curves at the pile base. Recognizing the limited number of *m-θ* curves available in the literature, this paper develops new theoretical curves using a rational two-dimensional horizontal pile/soil "slice" model to obtain improved representations of the stress and displacement fields in the soil around the pile. First, this model undergoes validation through comparisons with available linear-elastic solutions. Subsequently, it is employed in conjunction with a numerical discretization of the pile circumference to obtain nonlinear *m-θ* curves accounting for both soil yielding and slippage between pile and soil. The resulting curves are compared with a novel simplified solution based on an approximate distribution of vertical shear stresses at the pile/soil interface that can be derived in closed form. The new solutions are developed for undrained conditions considering elastic-perfectly plastic soil material behavior and properly accounting for slip at the pile/soil interface. **DOI: 10.1061/JGGEFK.GTENG-12889.**

Author keywords: Laterally-loaded piles; Monopile foundations; *m-θ* curves; Analysis.

Introduction

Traditional analysis methods for monopiles employ *t-z* and *p-y* curves to predict the nonlinear displacement response due to applied axial and lateral loads, respectively. The latter curves describe the distributed horizontal load-displacement response at any given depth and have been widely used for over 50 years in the offshore industry (McClelland and Focht 1956; Matlock 1970; Juirnarongrit and Ashford 2006; Basu and Salgado 2008; Franke and Rollins 2013; Khalili-Tehrani et al. 2014; Jeanjean et al. 2017; Byrne et al. 2020; Bateman et al. 2023a; Creasey et al. 2024). These developments have been summarized in books and reports (Scott 1981; Lam and Martin 1986; Reese and Van Impe 2011; Guo 2012; Viggiani et al. 2014; Favaretti et al. 2015; Poulos 2017; Vrettos 2021; Mylonakis and Crispin 2021; Kaynia 2021; Salgado 2022). A notable weakness of traditional *p-y* models lies in the omission of soil reaction mechanisms other than horizontal normal and shear stresses which tends to overpredict the lateral displacement response. This overprediction is particularly pronounced in squat monopiles (slenderness ratio $L/D < 10$) where additional resistance mechanisms are engaged, notably distributed bending moments along the pile due to vertical shear tractions generated from bending rotation (Byrne et al. 2017).

Although continuum solutions that inherently incorporate all relevant resistance mechanics are available (e.g., Basu et al. 2009; Han et al. 2017; Hu et al. 2022), improved solutions that retain the simplified 1D nature of the *p-y* analysis are preferred in routine design. A way to improve predictions from the *p*-y model is by considering the distributed moment-rotation response along the pile, known in the literature as *m-θ* curves (Sanchez-Salinero 1982; Lam and Martin 1986; Gerolymos and Gazetas 2006; Lam 2013; Agapaki et al. 2018; Byrne et al. 2020; Bateman 2025), as well as the horizontal force and moment resistance at the pile base (Osman et al. 2007; Lai et al. 2021; Fu et al. 2020; Byrne et al. 2020). The importance of accounting for these additional curves is evidenced by Murphy et al. (2018), who estimated that the supplementary soil reaction components (i.e., excluding the influence of *p-y* curves) may contribute a considerable 10%–25% to the overall pile resistance. Despite the extensive literature on *p-y* curves for different soil types and loading conditions, there has been limited investigation into developing corresponding distributed *m-θ* curves. Motivated by this lack in knowledge, this paper will focus on developing novel solutions for *m-θ* curves that define the distributed moment resistance (units of FL/L) due to the pile rotation at a specific depth.

Several early solutions focusing on elastic rotational springs and other equivalent distributed resistance mechanisms along flexible and rigid piles are available (Hetenyi 1946; Novak and Sheta 1980; Sanchez-Salinero 1982; Mylonakis 2000; Basu et al. 2009; Varun et al. 2009; Guo 2012; Agapaki et al. 2018). Following these efforts, empirical linear-elastic-perfectly plastic *m-θ* curves have recently been developed by Byrne et al. (2020), who calibrated idealized conic functions to results from nonlinear 3D finite-element analyses (FEA) of the full pile-soil system (by Zdravković et al. 2020). The FEA results were calibrated using medium-scale field test data in Cowden clay. The parametric study undertaken using those analyses resulted in simplified bilinear *m-θ* curves. However, as the analysis considers the full pile response, the *m-θ* curves are implicitly coupled with the calibrated *p-y* and base resistance curves, as well as additional geometric and material parameters and can hardly be viewed as self-standing solutions. Similar analyses have been conducted by Wan et al. (2021) using linear-elastic soil to obtain the initial stiffness of an *m-θ* curve. These

[1]Ph.D. Student, Dept. of Civil Engineering, Univ. of Bristol, Bristol BS8 1TR, UK (corresponding author). ORCID: https://orcid.org/0000-0003-3454-1756. Email: a.bateman@bristol.ac.uk

[2]Lecturer, Dept. of Civil, Maritime, and Environmental Engineering, Univ. of Southampton, Southampton SO16 7PN, UK; formerly, Postdoctoral Research Assistant, Dept. of Engineering Science, Univ. of Oxford, Oxford OX1 3PH, UK. ORCID: https://orcid.org/0000-0003-3074-8493

[3]Professor, Dept. of Civil and Environmental Engineering, Khalifa Univ., Abu Dhabi, UAE; University Chair in Geotechnics and Soil-Structure Interaction, Dept. of Civil Engineering, Univ. of Bristol, Bristol BS8 1TR, UK. ORCID: https://orcid.org/0000-0002-8455-8946

Note. This manuscript was submitted on April 3, 2024; approved on October 8, 2024; published online on February 27, 2025. Discussion period open until July 27, 2025; separate discussions must be submitted for individual papers. This paper is part of the ***Journal of Geotechnical and Geoenvironmental Engineering***, © ASCE, ISSN 1090-0241.

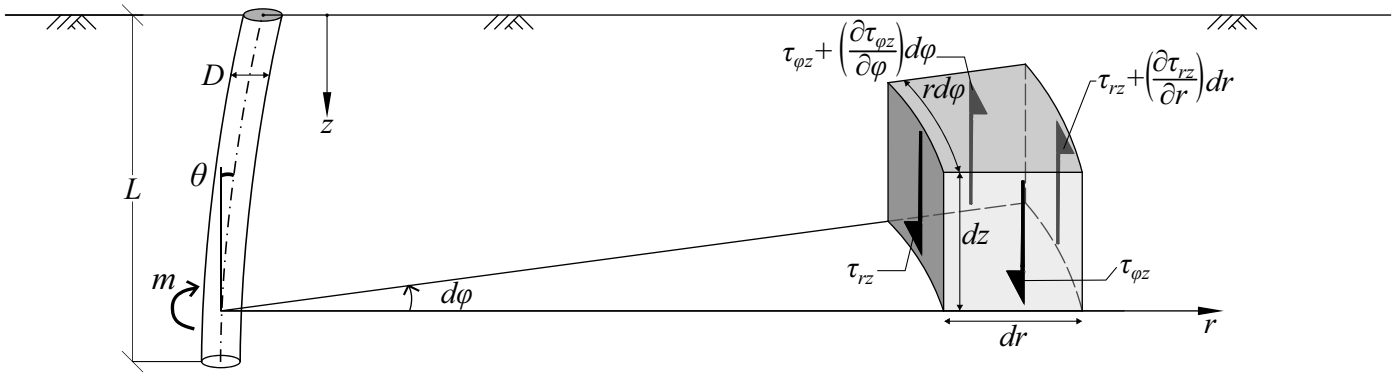

Fig. 1. Equilibrium of a soil element in axisymmetric mode due to pile slice rotation.

solutions both require calibration based on a specific pile-soil configuration using 3D FEA analysis.

Alternatively, some simplified analytical solutions for m-θ curves are available, framed by considering horizontal slices of the pile and soil medium and assuming there is negligible variation of interslice normal and shear stresses with depth, so each slice can be treated independently (plane strain model). Fig. 1 shows the vertical shear stresses, τ_{rz} and $\tau_{\varphi z}$ acting on an infinitesimal soil element within a horizontal slice. The m-θ curves are then formulated by calculating the contact shear stresses, τ_{rz}, developing at the pile periphery as a function of the bending rotation θ and summing the resultant distributed pile bending moment m at the specific depth.

A rigorous analytical solution for a linear-elastic material in two dimensions has been developed by Novak and Sheta (1980). This early solution assumes a horizontal soil/pile "slice" under plane deformation and establishes the m-θ curve based on an antisymmetric stress field at the pile circumference relative to the axis of rotation. This solution directly incorporates both vertical stress components τ_{rz} and $\tau_{\varphi z}$, but is limited to linear-elastic conditions. Alternatively, nonlinear vertical shear tractions developed at the pile periphery can be derived in an approximate manner using available t-z curves, describing the vertical shear stress and corresponding vertical displacement at the pile/soil interface (e.g., Kraft et al. 1981; Bateman et al. 2022b). Tott-Buswell and Prendergast (2022), and Bateman et al. (2023b) employed quadratic and power-law t-z curves, respectively, to obtain nonlinear m-θ curves. However, this approach considers an axisymmetric response mode, generating solely the stress component τ_{rz} and neglects the additional stresses, $\tau_{\varphi z}$, developing in antisymmetric mode.

A simpler relevant approach has been suggested by Fu et al. (2020), who compared the elastic stiffness of a t-z curve with that of an m-θ curve in dimensionless coordinates. This enabled a linear scaling factor to be obtained that can transform between the two curves. This method relies on the premise that the two curves are similar in shape and can be mapped onto a single "master" curve upon pertinent stretching or compression of coordinates, following analogous theories developed for p-y curves (Matlock 1970; Kagawa and Kraft 1981; Reese and Van Impe 2011). Alternative similarity factors have been developed from nonlinear quadratic and power-law t-z curves (Bateman et al. 2023b). In addition, Fu et al. (2020) extended this method to consider separate similarity factors for the elastic and plastic soil response by decomposing the overall shear strain into elastic and plastic components (two-part similarity). Following the original proposal by Skempton (1951), the similarity concept has also been used to relate stress–strain curves of a soil element test with t-z curves (Fu et al. 2020; Bateman et al. 2022a) as well as p-y curves (McClelland and Focht 1956; Matlock 1970; Reese and Van Impe 2011; Fu et al. 2020) and is still employed in modern offshore design (ANSI and API 2011).

The simplified analytical m-θ curves available in the literature enable straightforward, easy to apply solutions that are derived with clear assumptions and provide a time-efficient approach for preliminary design. Nonetheless, these analytical solutions exhibit a number of limitations. First, for nonlinear materials, the only shear stress considered in the derivation is τ_{rz}, neglecting the effect of the conjugate stress component $\tau_{\varphi z}$. Additionally, the effect of slip or a reduced shear strength at the pile/soil interface is often neglected as well as the yielding of the soil (or at least not explicitly considered). To account for the latter two effects, Jeanjean and Zakeri (2023) suggest using the conventional similarity factors from Fu et al. (2020) and then manually applying a cutoff moment to account for slip or soil yield. However, the value of the similarity factor is uncertain (Bateman et al. 2023b) and given that the two response modes are fundamentally different, it is not clear whether it is valid to assume similarity in shape between a t-z and an m-θ curve. Acknowledging these gaps in knowledge, this paper aims to improve upon the available analytical solutions by developing a novel nonlinear model encompassing both τ_{rz} and $\tau_{\varphi z}$ in the derivation of an m-θ curve for an elastic-perfectly plastic soil material.

To this end, existing analytical solutions are first investigated (including the derivation of nonlinear m-θ curves from available t-z curves) and their underlying assumptions and limitations are discussed. Second, a novel nonlinear model is developed in two dimensions by considering a horizontal pile/soil "slice" loaded antisymmetrically, leading to improved predictions for the vertical shear stresses τ_{rz} and $\tau_{\varphi z}$, and the associated soil displacements developing in the surrounding soil due to slice rotation. Third, based on the new model, a set of nonlinear m-θ curves are calculated for an elastic-perfectly plastic cohesive medium, encompassing the combined effects of slippage at the pile/soil interface and yielding of the soil mass. The full solution is obtained using a coupled system of equations that are formulated analytically and solved numerically. Finally, the full solution is compared with a novel approximate closed form solution developed in this paper based on a simplified shear stress distribution encompassing both the effect of slip at the pile/soil interface and the yielding of the soil.

Problem Definition

Developing m-θ curves is a complex boundary value problem that involves the coupling of soil resistances in multiple directions and depths. One approach to obtain useful solutions simplifies the three-dimensional continuum to two dimensions using a horizontal

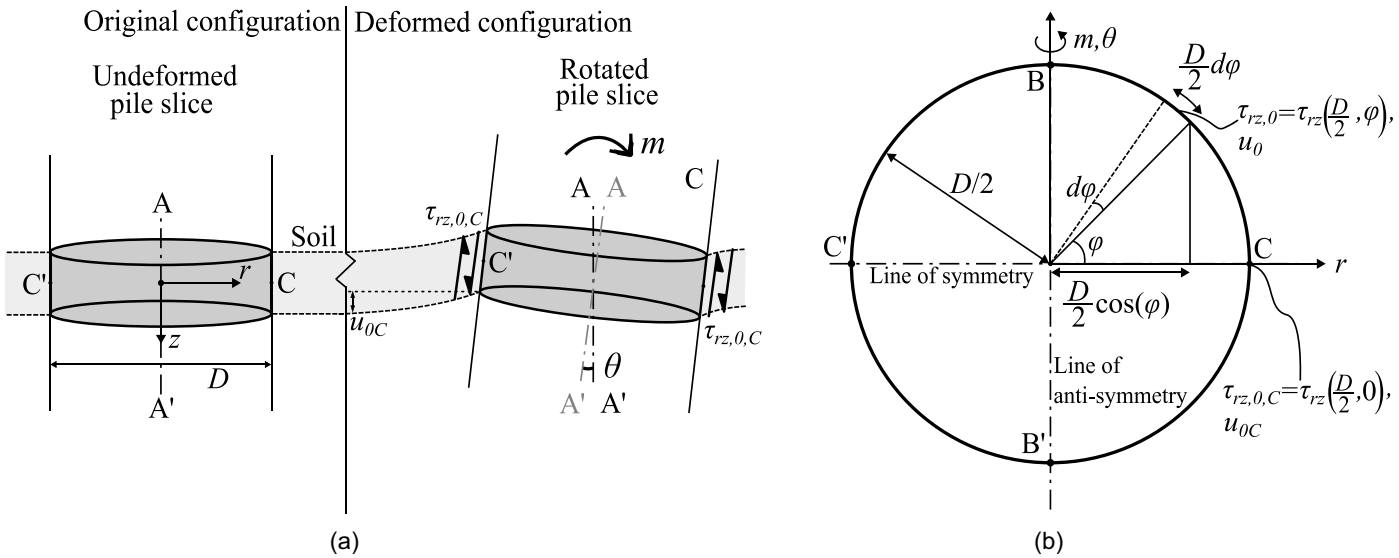

Fig. 2. Illustration of the horizontal pile slice problem, with reference to an m-θ curve: (a) side view; and (b) plan view. [Reprinted from Bateman et al. (2023b), under Creative Commons-BY-4.0 license (https://creativecommons.org/licenses/by/4.0/).]

pile/soil slice, as shown in Fig. 2. This simplification has been widely employed in relevant models to obtain p-y, m-θ, and t-z curves for lateral pile analysis under static and dynamic loads (e.g., Novak and Sheta 1980; Mylonakis 2001; Fu et al. 2020; Bateman et al. 2022b).

The pile segment shown in Fig. 2 is assumed to have a circular rigid cross section; henceforth, the geometry is described in cylindrical coordinates, where r is the radial distance from the pile centreline, z is the depth measured from the ground surface, and φ is the aperture angle measured anticlockwise from the location of maximum displacement ($\varphi = 0$). The pile segment is rotated in bending by an angle θ about an axis BB', perpendicular to and intercepting the pile's vertical axis (AA') as well as the centroid of the segment, resulting in an antisymmetric deformation pattern without net vertical displacement. This rotation applies a vertical shear stress, $\tau_{rz,0}(\varphi) = \tau_{rz}(D/2, \varphi)$, along the pile circumference. Assuming no preexisting vertical shear stresses, $\tau_{rz,0}$ is at its largest value, $\tau_{rz,0,C} = \tau_{rz,0}(0)$, at the intersection of the pile circumference with axis CC' and decreases with φ until it reaches zero at the intersection with the rotation axis BB' [i.e., $\tau_{rz,0}(\pi/2) = 0$]. This means that CC' is an axis of symmetry and BB' is an axis of antisymmetry for the observed shear stresses. To develop the model, the following assumptions are employed:

1. The domain is a two-dimensional horizontal pile-soil slice of infinitesimal thickness dz. Accordingly, the variation of normal stresses and displacements with depth is negligible, and thus, the corresponding normal strain, ε_{zz}, is zero.
2. The pile segment rotates, without translating, around the axis BB', orientated along the direction $\varphi = \pi/2$, which passes through its centroid resulting in an antisymmetric deformation pattern. Therefore, the tangential displacement u_φ and the corresponding shear strain $\gamma_{r\varphi}$ are zero.
3. The pile has a circular rigid cross section, meaning the vertical displacement at all points on the pile periphery can be determined as the product of the pile radius, the rotation angle θ, and the cosine of the aperture angle φ [see Eq. (2) below].
4. There are no preexisting vertical shear stresses in the soil.
5. As the slice undergoes pure rotation and the vertical shear stresses are independent of normal stresses, the p-y and m-θ curves are uncoupled.
6. Displacements, rotations, and associated strains are small.
7. Finally, total stress analysis is adopted under the assumption of zero apparent soil friction angle and uniform undrained shear strength, s_u, pertaining to clay soil under undrained conditions.

From this model, the distributed moment resistance of the pile slice for a specific rotation θ can be calculated as the summation of the vertical contact shear stresses acting on the pile periphery multiplied by their respective lever arm. Using cylindrical coordinates and considering both symmetry and antisymmetry, this can be written as:

$$m = 4\left(\frac{D}{2}\right)^2 \int_0^{\pi/2} \tau_{rz,0}(\varphi) \cos\varphi \, d\varphi \tag{1}$$

where m = distributed moment resistance (units of FL/L); D = pile diameter; and $\tau_{rz,0}(\varphi)$ = vertical contact shear stress at the pile/soil interface given as a function of the aperture angle φ, shown in Fig. 2.

Derivation Using t-z Curves

To calculate the distributed moment capacity of the pile slice using Eq. (1), the vertical contact shear stresses, $\tau_{rz,0}$, are required. From the geometry of the pile and given a rigid circular pile cross section, the vertical displacements of the pile at the pile periphery (assuming small rotation angles θ) can be given by

$$u_{0p} = \left(\frac{D}{2}\right)\theta\cos\varphi \tag{2}$$

where u_{0p} = vertical pile displacement around the pile circumference. Note, Eq. (2) also describes the vertical soil displacement at the pile periphery ($u_{0p} = u_0$) if there is perfect bonding between the pile and soil (i.e., no slip). However, the pile displacements, u_{0p}, is not equal to the soil displacement in the presence of slip at the pile circumference. Therefore, substituting this expression into Eq. (1) gives

$$m = 4\left(\frac{D}{2}\right)^2 \int_0^{\pi/2} \tau_{rz,0}(u_0(\varphi,\theta)) \cos\varphi \, d\varphi \tag{3}$$

which relies on the assumption of perfect bonding between the pile and soil.

If the contact shear stress $\tau_{rz,0}$ is known as a function of the soil displacements, u_0, a distributed m-θ curve can be derived. This expression describes a t-z curve, many of which are available in the literature (e.g., Fu et al. 2020; Tott-Buswell and Prendergast 2022; Bateman et al. 2023b). Specifically, t-z curves describe the vertical shear stress at the pile/soil interface $\tau_{rz,0}(u_0)$ resulting from a vertical displacement u_0. Substituting Eq. (2) into a t-z curve (Appendix I) gives the corresponding shear strain $\tau_{rz,0}$ as a function of θ and φ. Substituting this expression into Eq. (1) and integrating over φ enables an m-θ curve to be derived following Eq. (3).

As an example, a linear-elastic t-z curve can be given in the form [using Eq. (2)]

$$\tau_{rz,0} = k_v u_0 = k_v \left(\frac{D}{2}\right)\theta \cos\,\varphi \tag{4}$$

where k_v = stiffness of the linear t-z curve (units of F/L^2/L).

Substituting this expression into Eq. (3) yields an m-θ curve (before slip occurs)

$$m = \frac{\pi D^3}{8} k_v \theta = k_m \theta \tag{5}$$

where k_m = stiffness of the linear m-θ curve (units of FL/L).

Three t-z curves available in the literature are provided in the table in Appendix I, including two nonlinear solutions, followed by their corresponding m-θ curve. This approach is detailed further in Bateman et al. (2023b).

The solutions in the table in Appendix I assume perfect bonding at the pile/soil interface. However, it is inevitable that slip between the pile and soil will occur with increasing pile slice rotation. This can be modeled using a reduced interface strength $\tau_{rz,0} = \alpha s_u$ at the pile periphery, where α is an empirical adhesion factor discussed later in this paper. This condition of slip will first occur at $\varphi = 0$, where vertical pile displacement is maximum, and propagate around the pile circumference with increased slice rotation. This can be included in the derivation of the m-θ curve by defining φ_s (subscript s standing for "slip") as the maximum aperture angle at which the interface strength is reached (i.e., $\tau_{rz,0} = \alpha s_u$ and the pile/soil interface becomes bonded).

Considering the linear-elastic t-z curve in Appendix I, replacing u_0 from Eq. (2) ($u_0 = u_{0p}$ for perfect bonding between pile and soil) and setting $\tau_{rz,0} = \alpha s_u$ enables a function that relates the largest aperture angle at which slip occurs, defined here as φ_s, and the slice rotation, θ (Bateman et al. 2023b)

$$\cos\varphi_s = \frac{\alpha s_u}{\theta G} \ln\left(\frac{2r_m}{D}\right) \tag{6}$$

Therefore, using the linear-elastic t-z curve in Appendix I and considering slip at the pile/soil interface (for after slip first occurs; $\tau_{rz0,C} = \alpha s_u$), the corresponding m-θ curve can be derived in the form (Bateman et al. 2023b)

$$m = D^2 \alpha s_u \begin{cases} \dfrac{\pi - 2\varphi_s - \sin(2\varphi_s)}{4\ln\left(\frac{2r_m}{D}\right)}\left(\dfrac{G\theta}{\alpha s_u}\right) + \sin\varphi_s & \varphi_s < \pi/2 \\ 1 & \varphi_s = \pi/2 \end{cases} \tag{7}$$

While this approach enables incorporating soil nonlinearity and pile slip with relative ease, it relies on the assumption that the m-θ curve can be obtained based on a t-z curve. This hypothesis cannot be exact since the two problems involve different stress fields and symmetries.

Incorporation of Additional Shear Stresses

A set of solutions for this case can be obtained in terms of the pair of shear stresses, τ_{rz} and $\tau_{\varphi z}$, by considering the equilibrium of a soil element in the vertical direction. These coupled shear stresses are illustrated on an infinitesimal soil element in Fig. 1. Assuming the variation of normal stresses with depth is negligible, the vertical equilibrium of the soil element in cylindrical coordinates yields the governing equation

$$\frac{\partial(\tau_{rz} r)}{\partial r} + \frac{\partial \tau_{\varphi z}}{\partial \varphi} = 0 \tag{8}$$

which naturally depends on both r and φ. Introducing separation of variables, the two shear stresses can be written as products of independent functions of r and φ in the form:

$$\tau_{rz}(r,\varphi) = R_r(r)\Phi_r(\varphi) = \tau_{\text{ref}} \sum_{j=1,2,3\ldots}^{\infty} C_j \left(\frac{2r}{D}\right)^{-2j} \cos\left((2j-1)\varphi\right) \tag{9a}$$

$$\tau_{\varphi z}(r,\varphi) = R_\varphi(r)\Phi_\varphi(\varphi) = \tau_{\text{ref}} \sum_{j=1,2,3\ldots}^{\infty} C_j \left(\frac{2r}{D}\right)^{-2j} \sin\left((2j-1)\varphi\right) \tag{9b}$$

where R and Φ = functions of r and φ, respectively; j = harmonic parameter taking any positive integer value; C_j = dimensionless integration constants (Fourier coefficients) to be determined from the boundary conditions at the pile/soil interface; and τ_{ref} = reference shear stress that matches the units between the left and right-hand sides of the equations, rendering the integration constants dimensionless.

The full derivation of Eq. (9) from Eq. (8) is provided in Appendix II. It should be noted that these shear stresses are not derived for a specific soil constitutive model, apart from satisfying the weaker assumption that the soil shear stiffness is identical in both radial and tangential directions (i.e., $\tau_{rz}/\gamma_{rz} = \tau_{\varphi z}/\gamma_{\varphi z}$), yet not necessarily constant with level of strain and, therefore, is applicable even to nonlinear soil. However, the derivation of these equations does rely on three fundamental assumptions: first, due to symmetry, $\Phi_r(\varphi)$ and $\Phi_\varphi(\varphi)$ are even and odd periodic functions of φ, respectively, and can be written as sinusoidal and cosinusoidal harmonics. Second, following existing solutions (Novak and Sheta 1980), $R_r(r)$ and $R_\varphi(r)$ are assumed to be power-law functions of r. Third, soil is considered isotropic, so the same value of shear modulus G can be assumed for both conjugate shear strains, γ_{rz} and $\gamma_{\varphi z}$.

Linear-Elastic Soil

Retaining only the first term ($j = 1$) in Eq. (9), the functions reproduce the classical solution of Novak and Sheta (1980) for linear-elastic soil

$$\tau_{rz} = \tau_{rz,0,C}\left(\frac{D}{2r}\right)^2 \cos\varphi \tag{10a}$$

$$\tau_{\varphi z} = \tau_{rz,0,C}\left(\frac{D}{2r}\right)^2 \sin\varphi \tag{10b}$$

where $\tau_{rz,0,C} = \tau_{rz}(D/2, 0)$ = largest contact shear stress. Evidently, τ_{rz} and $\tau_{\varphi z}$ are strictly decreasing and increasing functions of φ in the interval $0 < \varphi < \pi/2$, attaining their maxima at $\varphi = 0$ and $\varphi = \pi/2$.

From Eq. (10*a*), the vertical soil displacements at the pile/soil interface, u_0, (at $r = D/2$) can be derived by integrating the vertical contact shear strains over r

$$\frac{u_0(\varphi)}{D} = \frac{1}{D}\int_{D/2}^{\infty} \gamma_{rz} dr = \left(\frac{\tau_{rz,0,C}}{2G}\right)\cos\varphi \tag{11}$$

Due to the rigidity of the pile slice and assuming perfect bonding between soil and pile (alternative assumptions are discussed later), u_0 can be set equal to the vertical displacements of the pile u_{0p}, which, in turn can be linked to pile rotation θ as in Eq. (2). Then, setting $\varphi = 0$ yields a value of $\tau_{rz,0,C}$ for a specific slice rotation

$$\tau_{rz,0,C} = G\theta \tag{12}$$

Further, the distributed moment acting on the pile slice can be calculated using Eq. (1), by integrating the contact stresses $\tau_{rz,0}$ from Eq. (10*a*) multiplied by their lever arm [length $(D/2)\cos\varphi$ in Fig. 2] around the pile periphery, to get

$$m = \frac{\pi}{4}\tau_{rz,0,C}D^2 = \frac{\pi}{4}GD^2\theta \tag{13}$$

which coincides with the solution by Novak and Sheta (1980) providing an elastic rotational stiffness $k_m = \pi GD^2/4$. This linear-elastic m-θ curve is plotted in Fig. 3(a) using different assumptions as to the distributed moment capacity cutoff to be discussed in the following sections.

Linear-Elastic Perfectly Plastic Soil

As a first approximation, $\tau_{rz,0}$ can be assumed to reach s_u at all points around the pile periphery [Fig. 3(b)]. By substituting $\tau_{rz,0} = s_u$ into Eq. (1) and integrating over φ yields an upper bound value of the distributed moment resistance m_u of $D^2 s_u$. Using this approximation is equivalent to applying a cutoff to the linear-elastic m-θ curve, shown as the upper plateau in Fig. 3(a).

However, the soil strength limit, s_u, should be applied to the magnitude of the shear stresses (i.e., the magnitude of the second stress invariant $\sqrt{J_2}$), rather than just $\tau_{rz,0}$, as follows:

$$\tau_{\text{mag}}(r,\varphi) = \sqrt{\tau_{rz}^2 + \tau_{\varphi z}^2} \le s_u \tag{14}$$

which corresponds to the radius of Mohr's circle on the $\sigma_1 - \sigma_3$ plane (Davies and Selvadurai 1996). To meet this criterion, if $\tau_{rz,0} = s_u$ at all aperture angles, then $\tau_{\varphi z,0}$ must equal zero, which is obviously not the case [Eq. (8)]. This would mean that simply applying the cutoff value $\tau_{rz,0} = s_u$ suggested would result in the magnitude of the shear stresses exceeding s_u along the periphery of the pile slice.

A simple approximate way to ensure Eq. (14) is satisfied, is by considering the elastic solution for shear stress given by Eq. (10) and limiting the resulting magnitude τ_{mag} to s_u. From Eq. (10), τ_{mag} yields

$$\tau_{\text{mag}}(r,\varphi) = \tau_{rz,0,C}\left(\frac{D}{2r}\right)^2 \tag{15}$$

which, remarkably, is independent of the aperture angle φ and decreases with radial distance from the pile circumference. Therefore, setting this equation equal to s_u at the pile periphery [$\tau_{\text{mag},0} = \tau_{\text{mag}}(D/2,\varphi) = s_u$] indicates that soil yield will occur at all locations on the pile periphery at once. This results in an elastic-perfectly plastic m-θ curve. Notably, $\tau_{rz,0}$ still varies with the aperture angle φ, shown in Fig. 3(b), and only equals s_u at $\varphi = 0$. Equating this $\tau_{rz,0,C}$ to that calculated in Eq. (12) yields the slice rotation at which soil first yields ($\tau_{\text{mag},0} = s_u$)

$$\theta_u = \frac{s_u}{G} \tag{16}$$

where θ_u = corresponding slice rotation at first soil yield.

The relevant ultimate distributed moment acting on the pile slice can be determined (neglecting pile slip; for $\alpha = 1$) by substituting this solution into Eq. (13) to get

$$m_u = \frac{\pi}{4}D^2 s_u \tag{17}$$

This distributed moment capacity is lower, by a factor of $\pi/4 \approx 0.79$, than simply providing the cutoff suggested previously based on the assumption $\tau_{rz,0} = s_u$ [Fig. 3(a)]. Interestingly, this approximate solution represents a rare case where the behavior is linear-elastic-perfectly plastic for both the constitutive model and the boundary value problem. In other words, Eqs. (16) and (17) correspond to rotations and moments under both yielding and

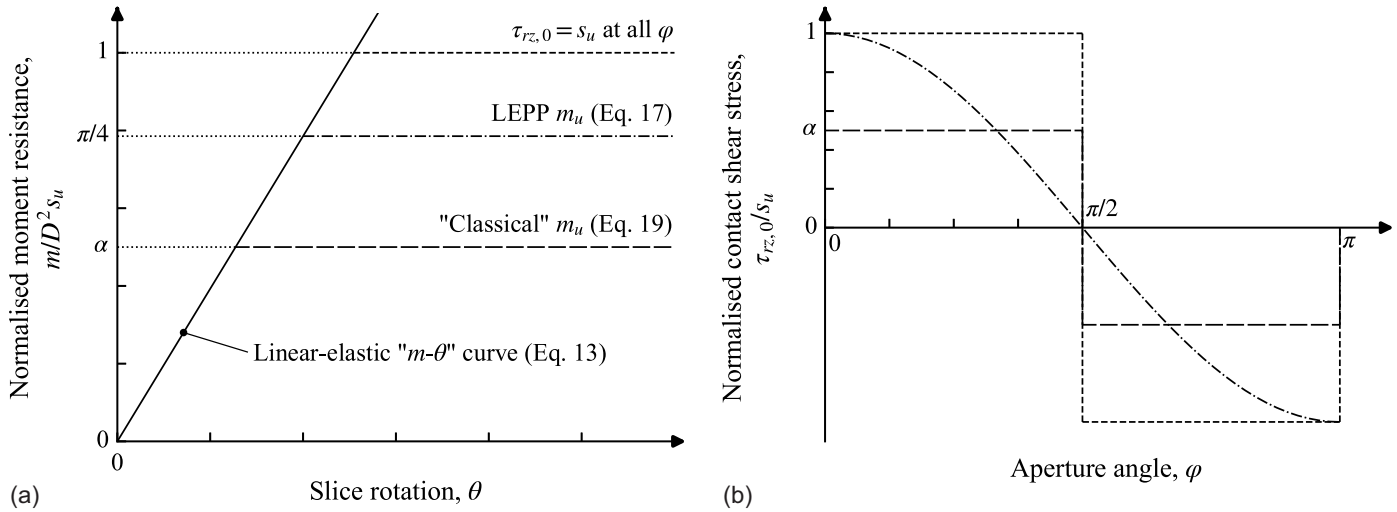

Fig. 3. (a) Linear-elastic and corresponding elastic-perfectly plastic m-θ curves based on different distributed moment capacity assumptions; and (b) assumed $\tau_{rz,0}$ for the different distributed moment capacities.

ultimate conditions [Fig. 3(a)]. Considering that in most soils, $G/s_u \approx 10^2$ to 10^3, θ_u is in the order of 10^{-3} to 10^{-2} radians (i.e., 0.06° to 0.6°) regardless of the absolute soil strength.

Slip at the Pile/Soil Interface

The shear strength of the interface between pile and soil may be lower than s_u. This is often referred to as "slip" and was originally introduced as a concept for axially loaded piles by Skempton (1959) to account for a reduced shear strength between soil and pile. This constraint limits the contact shear stresses around the pile periphery to a maximum value of $\tau_{rz,0} = \alpha s_u$ everywhere on the pile periphery, where α is an empirical adhesion factor and s_u is the soil undrained shear strength. Note that this specific condition does not limit $\tau_{\varphi z}$ since this is a failure of the interface, not of the soil itself. The relevant strength criterion can be written as

$$\tau_{rz,0} \leq \alpha s_u \tag{18}$$

To account for slip at the pile/soil interface, previous authors (e.g., Fu et al. 2020) suggest assuming a maximum value of $\tau_{rz,0} = \alpha s_u$ around the whole pile periphery [Fig. 3(b)]. Substituting this into Eq. (1) yields

$$m_u = D^2 \alpha s_u \tag{19}$$

which is referred to throughout as the "classical moment capacity" and, once again, acts as a manual cutoff value on the m-θ curve [Fig. 3(a)]. Since this cutoff value is generally lower than the soil yield value [Eq. (17); for $\alpha < \pi/4$], it would appear that the higher cutoff at soil yield will not be reached. However, from the discontinuity at $\varphi = \pi/2$ on Fig. 3(b), it is evident that the soil will reach yield before the interface slips at φ values approaching $\pi/2$. Therefore, the classical moment capacity in Eq. (19) would only be possible if soil yield is not considered explicitly in the solution, indicating it is an overestimate of the capacity.

In reality, the condition of slip will first occur at $\varphi = 0$ and propagate around the pile circumference with increased slice rotation. Incorporating both slip and yield into this model is not trivial since the shear stresses need to be defined everywhere on the pile periphery after slip first occurs, which cannot be captured by these approximate solutions.

General Solution

The general solutions for shear stresses τ_{rz} and $\tau_{\varphi z}$ in Eq. (9) can be employed to calculate the m-θ curve for a linear-elastic perfectly plastic (LEPP) material. This analysis will also consider a pile/soil interface strength of $\tau_{rz,0} = \alpha s_u$ to incorporate slip at the pile periphery as well as soil yielding. The herein proposed analysis does not enable an m-θ curve to be derived in closed form since the dimensionless Fourier constants C_j are unknown and need to be obtained from the numerical solution of a system of coupled linear equations. The general solution consists of three parts. First, before either soil yield ($\tau_{\text{mag}} < s_u$) or slip at the interface occurs ($\tau_{rz,0} < \alpha s_u$), the solution is equivalent to that for an elastic material, providing an m-θ curve given by Eq. (13) using a single harmonic. Second, once slip starts to occur ($\tau_{rz,0,C} = \alpha s_u$), but the magnitude of shear stresses is below yield [$\tau_{\text{mag}} < s_u$; according to Eq. (14)], the solution becomes nonlinear and requires considering a full set of harmonic coefficients $j = 1$ to N. Third, once soil yielding also occurs [$\tau_{\text{mag}} = s_u$; according to Eq. (14)], the nonlinear solution needs to be modified accordingly.

Incorporation of Slip at the Pile/Soil Interface

The criterion of slip limits the vertical contact shear stresses at the pile/soil interface, $\tau_{rz,0}$, to a reduced shear strength of αs_u as expressed by Eq. (18). A value of φ_s is defined as the largest aperture angle at which the shear stresses at the pile/soil interface equal αs_u and is used as the main independent variable in this analysis. In the region $0 < \varphi < \varphi_s$, it holds that $\tau_{rz,0} = \alpha s_u$ and is referred to as the "slipped" region [arc CS; Fig. 4(a)].

In the region of perfect bonding ($\varphi_s < \varphi < \pi/2$), known herein as the "bonded" region [arc SB in Fig. 4(a)], the vertical soil displacements can be obtained from the integration of soil shear strain γ_{rz} over r

$$u_0(\varphi) = \int_{D/2}^{\infty} \gamma_{rz} dr = \frac{s_u}{G}\left(\frac{D}{2}\right) \sum_{j=1,2,3\ldots}^{\infty} \frac{C_j}{2j-1} \cos\left((2j-1)\varphi\right) \tag{20}$$

Setting this equation equal to the pile displacements in Eq. (2), valid for the bonded region ($\varphi_s < \varphi < \pi/2$), and introducing pile

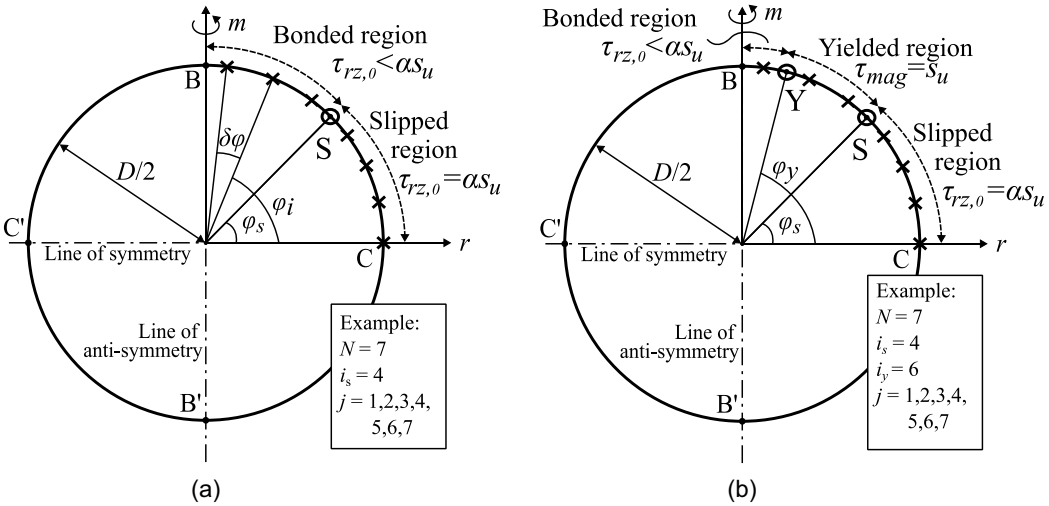

Fig. 4. Illustration of the discretization of the pile: (a) before soil yield; and (b) after soil yield.

rotation θ, the following equation for the pile slice rotation as a function of φ_s can be derived

$$\theta(\varphi_s) = \frac{s_u}{G\cos(\varphi_s)} \sum_{j=1,2,3\ldots}^{\infty} \frac{C_j}{2j-1}\cos\left((2j-1)\varphi_s\right) \tag{21}$$

Due to the infinite series involved, it is not possible to obtain an m-θ curve in closed form using the shear stresses in Eq. (9). Instead, a numerical solution is sought by discretizing a quarter of the pile circumference into N discretization points, each corresponding to a distinct arbitrary angle φ_i, illustrated in Fig. 4(a).

To calculate the distributed moment resistance for any given φ_s value (and therefore a corresponding θ angle), the following analysis procedure should be followed. First, the Fourier coefficients C_j are calculated by solving a system of equations, $\boldsymbol{FC} = \boldsymbol{V}$, where $\boldsymbol{F}$ is a $N \times N$ square, nonsymmetric matrix of components relating to i sums of j products of C_j terms (combined as vector $\boldsymbol{C}$) and $\boldsymbol{V}$ is a vector of values these sums equal. Second, given C_j, the shear stresses, τ_{rz} and $\tau_{\varphi z}$, are calculated around the pile periphery using Eq. (9), and it is checked that $\tau_{\text{mag}} < s_u$ [Eq. (14)] is true everywhere. If this condition is not met, soil yield should be considered (see the following section). Finally, the distributed moment resistance m for a specific pile rotation is calculated from τ_{rz} using Eq. (1). As the governing equations are perfectly satisfied everywhere in the soil medium, yet only at the discretization points along the pile periphery, the solution can be classified as a collocation approach.

Matrix $\boldsymbol{F}$ consists of the terms $f_b(i,j)$ and $f_s(i,j)$ that correspond to the bonded and slipped regions according to Eqs. (22*a*) and (23*a*). These are made up of the jth term in a sum relating to the ith discretization point (where $\varphi = \varphi_i$). The $f_b(i,j)$ terms result from equating the pile and soil displacements at the interface, while the $f_s(i,j)$ terms result from $\tau_{rz,0} = \alpha s_u$ in the slipped region. Vector $\boldsymbol{V}$ consists of terms $V_b(i)$ and $V_s(i)$ that correspond to the respective solutions of $f_b(i,j)$ and $f_s(i,j)$ according to Eqs. (22*b*) and (23*b*) (see Appendix III for more details)

$$f_b(i,j) = \frac{1}{2j-1}\left[\cos\left((2j-1)\varphi_i\right) - \frac{\cos\varphi_i}{\cos\varphi_s}\cos\left((2j-1)\varphi_s\right)\right] \tag{22a}$$

$$V_b(i) = 0 \tag{22b}$$

$$f_s(i,j) = \cos\left((2j-1)\varphi_i\right) \tag{23a}$$

$$V_s = \alpha \tag{23b}$$

An assumed value of φ_s is selected as between two successive discretization points on the pile periphery. For simplicity and numerical stability, φ_s is defined here as halfway between two discretization points [note that Eq. (22) becomes trivial for $\varphi_i = \varphi_s$]. Interestingly, the solution to the system of simultaneous equations depends only on the selected values of φ_s and α. The value of N dictates the number of j values incorporated within the infinite sums. It has been found by the authors that this has minimal effect on the results beyond approximately $N = 10$. Solutions shown in this paper use $N = 250$ to yield smooth m-θ curves, that can be viewed as essentially exact results in the realm of the analysis assumptions at hand. These steps should be repeated for multiple φ_s values [and therefore corresponding θ angles according to Eq. (21)] to obtain the full m-θ curve. An m-θ curve developed using this method is plotted in Fig. 5(a) (results neglect soil yield). The minor error resulting from the use of the classical cap in Eq. (19) is worthy of note.

Solution after Soil Yield

To incorporate soil yield in this solution, τ_{mag} should be limited to s_u according to Eq. (14). To account for this, an additional angle $\varphi_y (> \varphi_s)$ is defined as the aperture angle below which (outside the slipped region) the soil yields, as illustrated in Fig. 4(b). Accordingly, a third region needs to be introduced between the slip and the bonded regions (i.e., $\varphi_y > \varphi > \varphi_s$), referred to herein as the "yielded" region [arc SY in Fig. 4(b)].

Within the yielded region [arc SY in Fig. 4(b)], it is known that $\tau_{\text{mag}} = s_u$ and thus $\partial\tau_{\text{mag}}/\partial\varphi = 0$. The latter equation is advantageous over the former for the purposes of this analysis, as it enables a system of linear equations in terms of C_j to be set up. When yield is considered, Matrix $\boldsymbol{F}$ consists of the terms $f_b(i,j)$, $f_s(i,j)$ as before [Eqs. (22*a*) and (23*a*)] as well as $f_y(i,j)$ within the yielded region determined from the constraint in Eq. (24*a*) (see Appendix IV for more details). Similarly, Vector $\boldsymbol{V}$ corresponds to the respective solution, given by Eqs. (22*b*), (23*b*), and (24*b*)

$$f_y(i,j) = (2j-1)\left[\left(\frac{\tau_{\varphi z}}{\tau_{rz}}\right)\cos\left((2j-1)\varphi_i\right) - \sin\left((2j-1)\varphi_i\right)\right] \tag{24a}$$

$$V_y = 0 \tag{24b}$$

Note that as the shear stress ratio $(\tau_{rz}/\tau_{\varphi z})$ is not known a priori, Eq. (24) is a nonlinear function of C_j. Nevertheless, for sufficiently dense discretization [$N > 20$ so $\delta\varphi$ in Fig. 4(a) is small], it can be assumed that $(\tau_{rz}/\tau_{\varphi z})$ does not vary significantly between successive analysis steps (φ_y located at the previous discretization point) and can be taken as equal to the value calculated at the same φ_i during the previous analysis step.

To obtain the m-θ curve once τ_{mag} first reaches s_u anywhere on the pile circumference, the following analysis procedure should be followed. First, assume φ_s does not increase relative to the previous step. Second, assume a φ_y value as equal to the φ_i one discretization point further than either the φ_s or the previously assumed yield point φ_y. Third, calculate the Fourier coefficients C_j by solving the aforementioned system of equations. Fourth, use the calculated C_j values to determine the shear stresses τ_{rz} and $\tau_{\varphi z}$ using Eq. (9) at the pile periphery. From here, the shear stress ratio $(\tau_{rz}/\tau_{\varphi z})$ and τ_{mag} can be established. Finally, if $\tau_{\text{mag}}/s_u < 1$ in the region of $\varphi_s < \varphi_i < \varphi_y$, then increase φ_s by one discretization point and repeat the presented steps.

This simple procedure should be repeated for multiple values of φ_y to obtain the full m-θ curve. An example of Python implementation of this approach is provided in the Supplemental Materials. The solution is plotted in Fig. 5(a) and demonstrates that incorporating soil yield into the general formulation has a negligible effect on the final m-θ curves for approximately $\alpha < 0.7$. Beyond the specific value, soil yield becomes gradually much more important due to increased interface strength and yields more conservative values for peak strength m_u than Eq. (19).

Despite existing research demonstrating the importance of considering m-θ curves when investigating the response of monopiles (Byrne et al. 2017; Murphy et al. 2018), a very limited number of such curves are available in the literature. A comparison of the m-θ curves produced using this solution against those calibrated from the PISA tests (Byrne et al. 2020) is provided in Fig. 5(b). To better fit pile response, integrated analysis methods like PISA employ a two-stage calibration process that, after selecting individual soil reaction curves (including corresponding p-y, $H_b - v_b$, and $M_b - \theta_b$ curves) from an FE analysis, adjusts them to best match the measured

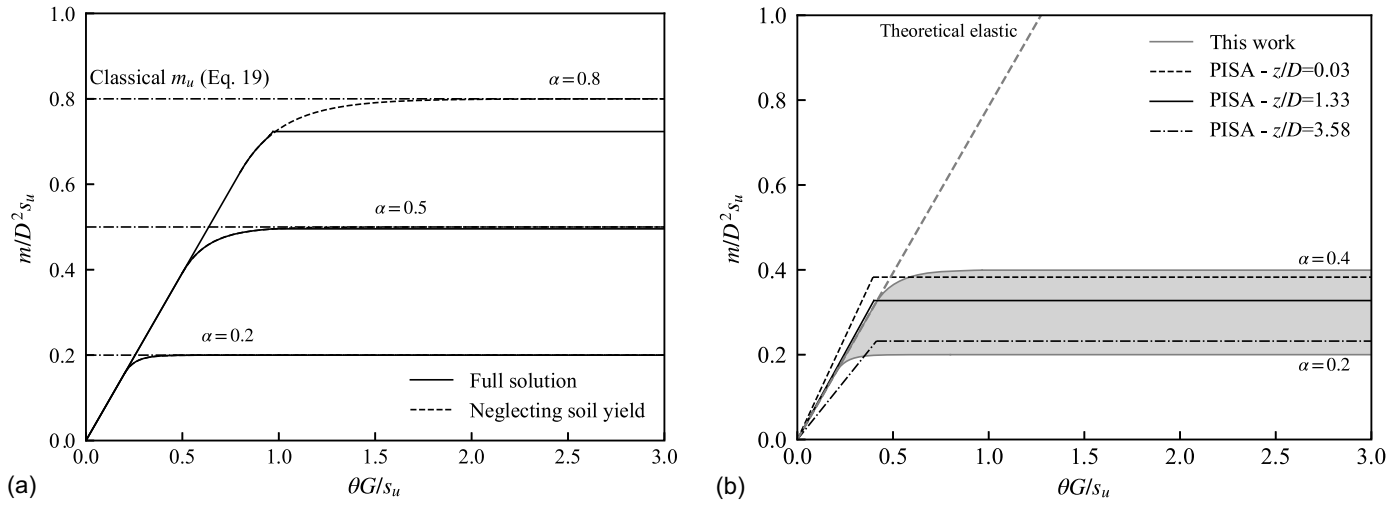

Fig. 5. (a) m-θ curves obtained from the general solution compared with the general solution neglecting soil yield; $N = 250$; and (b) comparison of the m-θ curves derived in this work (grey; hatched area) against those calibrated with the PISA tests in Byrne et al. (2020) (black).

global pile response. In the author's view, this empirical adjustment means that the improved curves in the PISA solution cannot be viewed as stand-alone solutions for m-θ curves. Instead, Fig. 5(b) shows the first stage calibration results that, despite being inherently coupled with the other soil reaction curves through the calibration process, compare well with the results from this work. Note that the PISA results do not correspond to specific values of α as in the theoretical solution.

Following the approach described in this section, the variation of τ_{rz}, $\tau_{\varphi z}$, and τ_{mag} around the pile circumference can be plotted for three different loading stages, as shown in Fig. 6. As expected, τ_{rz} reaches αs_u before τ_{mag} reaches s_u. This figure demonstrates that τ_{rz} is limited to αs_u and τ_{mag}/s_u is limited to 1. Note after soil yield first occurs, φ_s in the general solution can keep increasing and all response parameters exhibit strong gradients near the threshold angles φ_s and φ_y. Importantly, $\tau_{rz}/\tau_{\varphi z}$ does not change significantly at high φ values after yield first occurs. These shear stresses are compared with the simplified solution in the following section.

Simplified Solution

Since the general solution presented above is not trivial and does not yield an m-θ curve in closed form, deriving a simpler solution is desirable. To this end, it can be assumed that τ_{rz} after slip first occurs (i.e., $\tau_{rz,0,C} = \alpha s_u$) can be approximated by the following function:

$$\tau_{rz}(r,\varphi) = \alpha s_u \left(\frac{D}{2r}\right)^2 \begin{cases} 1, & \varphi \le \varphi_s \text{ (slipped)} \\ \dfrac{\cos\varphi}{\cos\varphi_s}, & \varphi > \varphi_s \text{ (bonded)} \end{cases} \tag{25}$$

which reduces to the elastic solution when $\varphi_s = 0$ and reproduces the features of the general solution (Fig. 6).

Similar to the general solution, a value of φ_s is defined as the boundary between the slipped and bonded regions—i.e., the largest aperture angle at which the shear stresses at the pile/soil interface equal the soil strength. Thus, for $0 < \varphi < \varphi_s$ (slipped region; arc CS on Fig. 7) slip has occurred and $\tau_{rz,0}$ is limited to αs_u; whereas, for $\varphi_s < \varphi < \pi/2$ (bonded region; arc SB on Fig. 7) there is perfect bonding meaning $\tau_{rz,0} < \alpha s_u$, see Fig. 6.

First, for $\tau_{rz,0,C} < \alpha s_u$, the solution for a perfectly elastic soil can be employed, resulting in an m-θ curve given by Eq. (13). This equation is valid up to a rotation of

$$\theta_s = \frac{\alpha s_u}{G} \tag{26}$$

where θ_s = pile slice rotation at which slip at the pile/soil interface first occurs (i.e., $\tau_{rz,0,C} = \alpha s_u$).

Beyond the first slip, the vertical displacements of the soil at the pile/soil interface, u_0, (at $r = D/2$) can be derived for any aperture angle φ by integrating the shear strain over r

$$u_0(\varphi) = \int_{D/2}^{\infty} \gamma_{rz} dr = \frac{\alpha s_u}{G}\left(\frac{D}{2}\right) \begin{cases} 1 & \varphi \le \varphi_s \text{ (slipped)} \\ \dfrac{\cos\varphi}{\cos\varphi_s} & \varphi > \varphi_s \text{ (bonded)} \end{cases} \tag{27}$$

By equating this equation of soil displacement with the known pile slice displacements, given by Eq. (2), in the bonded region (arc PB on Fig. 7), φ_s as a function of the slice rotation can be calculated

$$\cos\varphi_s = \frac{\alpha s_u}{G}\left(\frac{1}{\theta}\right) \tag{28}$$

Finally, the distributed moment acting on the pile slice can be determined by integrating the contact stresses $\tau_{rz,0}(\varphi)$ multiplied by their lever arm along the pile periphery using Eq. (1)

$$m = \frac{\alpha s_u D^2}{2}\left[\sin\varphi_s + \frac{\pi/2 - \varphi_s}{\cos\varphi_s}\right] \tag{29a}$$

where φ_s is given in Eq. (28). Substituting φ_s into Eq. (29) yields the explicit solution

$$m = \frac{D^2 \alpha s_u}{2}\left[\sqrt{1 - \left(\frac{\alpha s_u}{G\theta}\right)^2} + \frac{G\theta}{\alpha s_u}\left[\frac{\pi}{2} - \arccos\left(\frac{\alpha s_u}{G\theta}\right)\right]\right] \tag{29b}$$

Remarkably, this result is identical to that derived directly from t-z curves based on different assumptions [Eq. (7)], if one assumes $\ln(2r_m/D) = 1$. Note that this result is valid after the slip first occurs and before the soil yields. To be able to calculate the rotation at which the soil yields, first, a function for $\tau_{\varphi z,0}$ must be introduced.

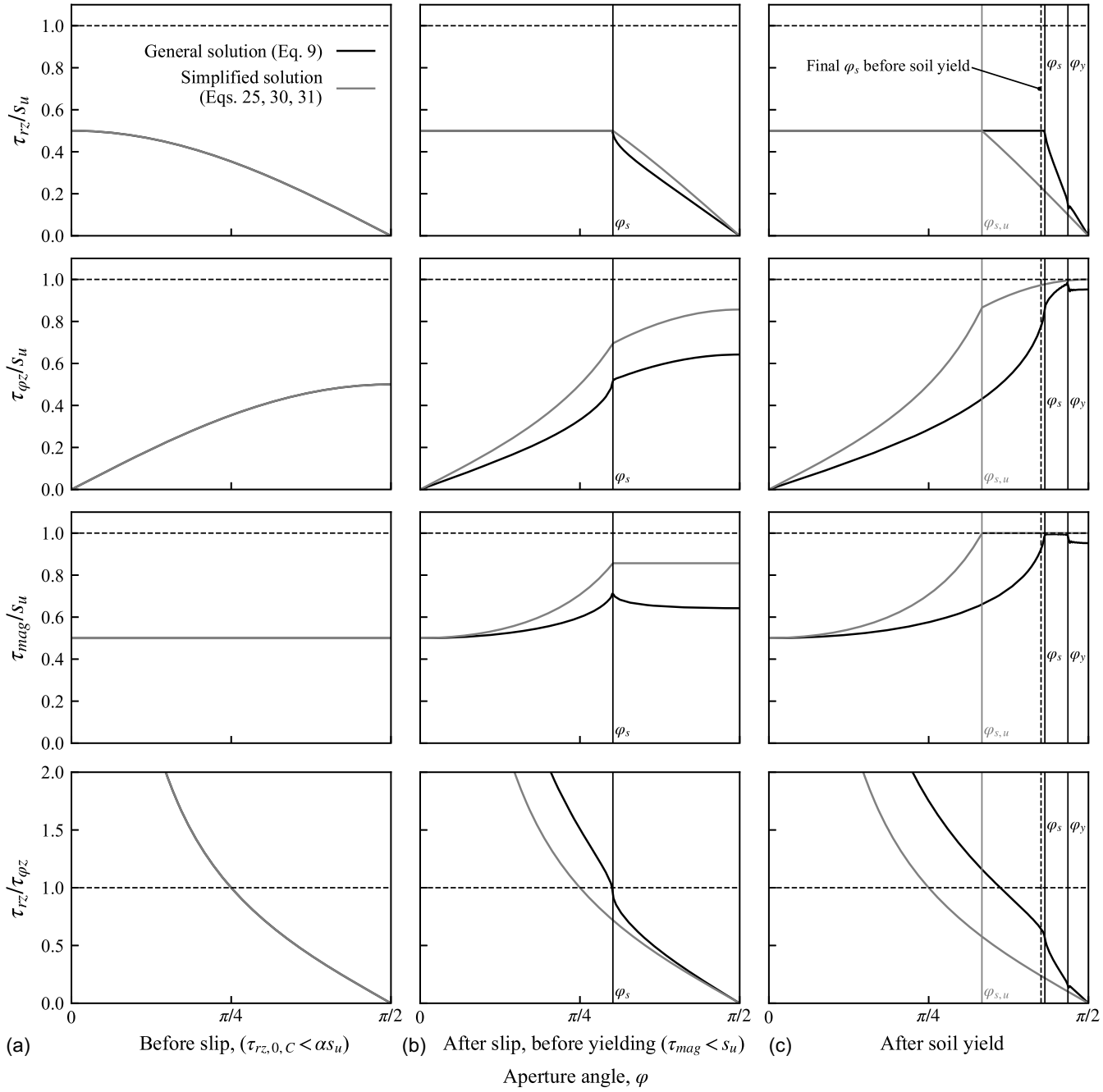

Fig. 6. Variation of shear stresses around the pile circumference comparing the general solution with the simplified solution for: (a) just before slip occurs; (b) before soil yield ($\tau_{\text{mag}} < s_u$); and (c) after soil yield ($\alpha = 0.5$, $N = 250$).

By substituting τ_{rz} in Eq. (25) into the vertical equilibrium conditions [Eq. (8)], it can be readily established that $\tau_{\varphi z,0}$ after slip first occurs can be given by [also in the form presented in Eq. (9)]

$$\tau_{\varphi z,0}(\varphi) = \alpha s_u \begin{cases} \tan\varphi, & \varphi \le \varphi_s \text{ (slipped)} \\ \dfrac{\sin\varphi}{\cos\varphi_s}, & \varphi > \varphi_s \text{ (bonded)} \end{cases} \tag{30}$$

This shear stress is compared with those from the general solution in Fig. 6. This shows that the approximate solution gives slightly higher values than those obtained from the general solution. From both vertical shear stresses at the pile periphery, $\tau_{rz,0}$ and $\tau_{\varphi z,0}$, [Eqs. (25) and (30)], the magnitude of the shear stresses can be calculated after the slip first occurs (i.e., $\tau_{rz,0,C} = \alpha s_u$):

$$\tau_{\text{mag},0}(\varphi) = \alpha s_u \begin{cases} \dfrac{1}{\cos\varphi} & \varphi \le \varphi_s \text{ (slipped)} \\ \dfrac{1}{\cos\varphi_s}, & \varphi > \varphi_s \text{ (bonded)} \end{cases} \tag{31}$$

From this equation, it can be seen that $\tau_{\text{mag},0}$ will not reach s_u before $\tau_{rz,0,C} = \alpha s_u$ given an α value of less than 1. Thus, a slip will occur before any of the soil yields.

Additionally, based on the $\tau_{\varphi z,0}$, it can be shown from Eq. (31) that the soil will yield first in the bonded region (arc PB in Fig. 7, $\varphi > \varphi_s$) which is again independent of φ. Therefore, the maximum possible value of φ_s according to this solution can be given by

$$\cos\varphi_{s,u} = \alpha \tag{32}$$

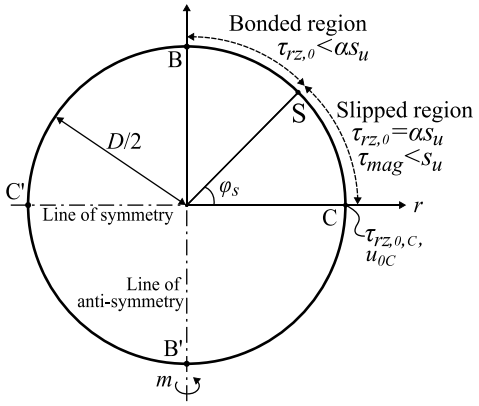

Fig. 7. Illustration of the occurrence of slip ($\tau_{rz} = \alpha s_u$) and soil yield ($\tau_{\text{mag}} = s_u$) around the pile/soil interface and the definition of φ_s and φ_y in the simplified solution.

where $\varphi_{s,u}$ = value of φ_s when the soil yields and is the maximum possible value of φ_s for this simplified solution. The variation of φ_s with pile slice rotation is shown in Fig. 8.

This value of $\varphi_{s,u}$ occurs initially at a pile slice rotation of θ_u ($\tau_{\text{mag}} = s_u$)

$$\theta_u = \frac{s_u}{G} \tag{33}$$

Once soil yield has occurred in the bonded region (arc SB from Fig. 7) stresses in the soil will remain constant. Therefore, the ultimate distributed moment capacity, m_u, of the pile slice incorporating pile slip and after the soil has yielded can be given by

$$m_u = \frac{s_u D^2}{4}\left[2\alpha\sqrt{1-\alpha^2} - 2\arccos(\alpha) + \pi\right] \tag{34}$$

Notably, this ultimate distributed moment capacity is once again lower than the anticipated value of $D^2 s_u$ and, as expected, is lower than when slip is ignored (assuming $\alpha < 1$). Therefore, the full

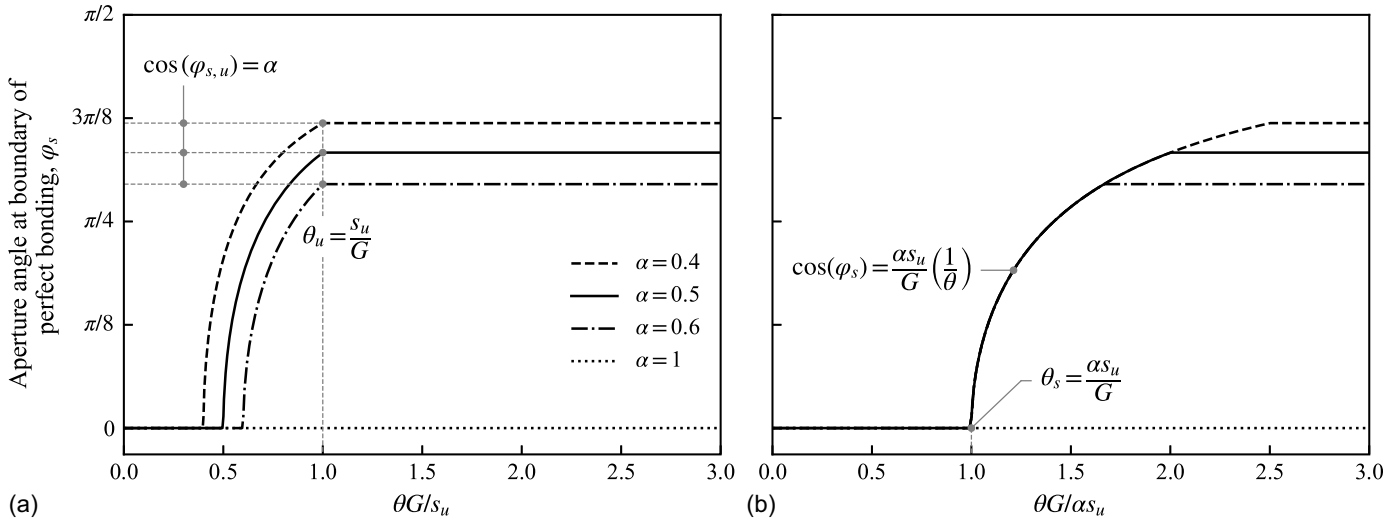

Fig. 8. Variation of φ_s with pile slice rotation in the simplified solution [Eqs. (28) and (32)]. Pile slice rotation (x-axis) is normalized by: (a) G/s_u; and (b) $G/\alpha s_u$.

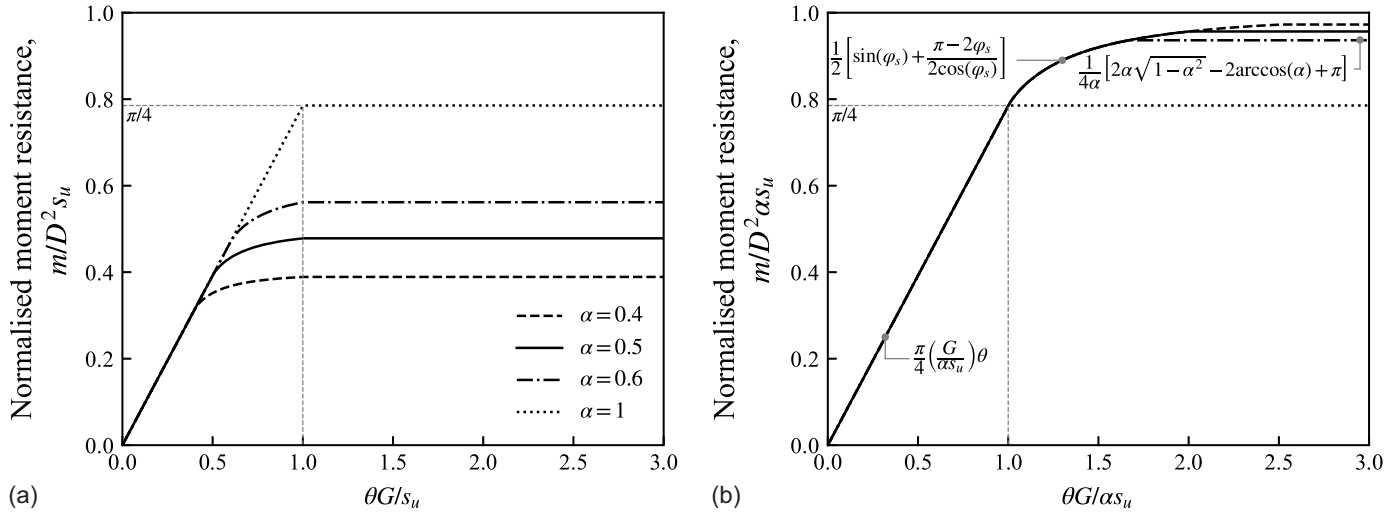

Fig. 9. m-θ curve derived using the simplified solution assuming a pile/soil interface strength of $\tau_{rz,0} = \alpha s_u$ [Eq. (35)]. Axes normalized by: (a) s_u; and (b) αs_u.

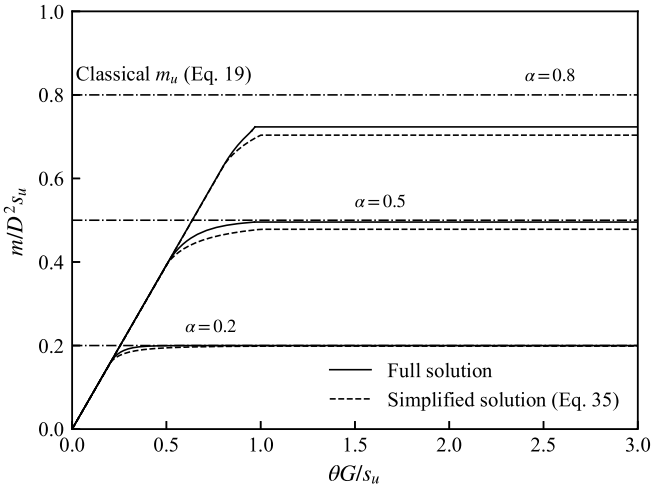

Fig. 10. m-θ curves obtained from the simplified solution [Eq. (35)] compared with the general solution incorporating soil yield ($N = 250$).

simplified m-θ curve can be written as a combination of Eqs. (13), (29), and (34)

$$\frac{m}{D^2 \alpha s_u} = \begin{cases} \frac{\pi}{4}\left(\frac{G\theta}{\alpha s_u}\right) & \theta \le \frac{\alpha s_u}{G} \\ \frac{1}{2}\left[\sqrt{1-\left(\frac{\alpha s_u}{G\theta}\right)^2} + \frac{G\theta}{\alpha s_u}\left[\frac{\pi}{2} - \arccos\left(\frac{\alpha s_u}{G\theta}\right)\right]\right] & \frac{\alpha s_u}{G} < \theta \le \frac{s_u}{G} \\ \frac{1}{4\alpha}\left[2\alpha\sqrt{1-\alpha^2} - 2\arccos(\alpha) + \pi\right] & \theta > \frac{s_u}{G} \end{cases} \tag{35}$$

Eq. (35) reproduces the "classical" ultimate moment resistance [Eq. (19)] when α tends to 0 and also reproduces the elastic-perfectly plastic response when $\alpha = 1$.

This simplified solution enables a closed form result (plotted in Fig. 9) using two different normalizations for each axis. A comparison against the general solution considering soil yield is provided in Fig. 10. This solution is shown to be a very close match to the general result with the maximum distributed moment approximately 3% more conservative (when $\alpha = 0.8$) than the general solution. For smaller values of α, the discrepancy is even smaller.

Summary and Conclusions

Analyzing the distributed moment-rotation response of a thin pile/soil slice, known as an m-θ curve, is important when predicting the response of monopile foundations. Despite the importance of these curves in design, few m-θ curves are available in the literature. Motivated by this lack of solutions, this paper has developed a set of novel improved analytical expressions for m-θ curves using the pile/soil slice approach considering an elastic-perfectly plastic soil material and a total stress failure criterion pertaining to undrained conditions. The solutions are cast in the form of infinite sums of Fourier components derived from vertical equilibrium considerations [Eq. (9)]. These are validated against the classical solutions of Novak and Sheta (1980) for an elastic material [Eq. (13)].

Furthermore, to incorporate soil yield into this solution, the magnitude of the shear stresses [Eq. (14)] was limited to the undrained shear strength of the soil, s_u. This results in soil yield occurring at all locations on the pile periphery at once, at a slice rotation $\theta_u = s_u/G$ and represents a rare case where the behavior is linear-elastic-perfectly plastic for both the constitutive model and the boundary value problem. The distributed moment capacity of the pile slice resulting from this solution is $m_u = \pi D^2 s_u/4$, which acts as an upper bound of the true distributed moment capacity of the pile slice.

Slip at the pile/soil interface was incorporated through a reduction factor on the interface strength [the factor α in Eq. (18)]. Previous authors have suggested that the distributed moment capacity can be calculated by assuming $\tau_{rz,0} = \alpha s_u$ holds at all locations around the pile periphery. This results in the "classical moment capacity" $m_u = \alpha D^2 s_u$ that was shown to overestimate the capacity since soil yield is neglected.

A more general semianalytical solution was developed that incorporates both soil yield and slip at the pile/soil interface. This solution shows that incorporating soil yield has a negligible effect for $\alpha < 0.7$. Beyond this threshold, soil yield becomes gradually more important due to the increased interface strength. Further, the theoretical formulation has demonstrated that the nonlinear pile-soil contact problem can be solved in an exact manner using the superposition of harmonics, a trait typically associated with linear solutions.

Finally, this paper presents novel derived m-θ curves in closed form using the first term of the shear stress functions that incorporate both soil yield and slip at the pile/soil interface [Eq. (35)]. The capacity obtained from this solution is a very close match to the general solution, providing more conservation results by a mere 3%. Furthermore, this solution reproduces the approximate "classical moment capacity" result when α tends to 0 and the elastic-perfectly plastic result when α tends to 1.

Appendix I. m-θ Curves Neglecting Slip, Derived from Available t-z Curves Using Eq. (1)

Soil constitutive model	t-z curve	m-θ curve
Linear	$\tau_{rz,0}(\varphi) = \frac{2u_0}{D} G\left[\ln\left(\frac{2r_m}{D}\right)\right]^{-1}$ (Randolph and Wroth 1978)	$m = \frac{\pi D^2}{4} G\left[\ln\left(\frac{2r_m}{D}\right)\right]^{-1}\theta$ (Bateman et al. 2023b)
Power-law	$\tau_{rz,0}(\varphi) = \frac{s_u}{2}\left[\frac{2u_0}{D}\left(\frac{1-b}{\gamma_{50} b}\right)\right]^b$ (Vardanega et al. 2012)	$m = \frac{D^2 s_u}{4}\left(\frac{1-b}{\gamma_{50} b}\right)^b \mathrm{B}\left(\frac{1}{2}, \frac{b+2}{2}\right)\theta^b$ (Bateman et al. 2023b)
Quadratic	$\tau_{rz,0}(\varphi) = G_0\left(\frac{u_0}{2D}\right)\left[1 - \frac{G_0}{8 s_u}\left(\frac{u_0}{D}\right)\right]$ (Randolph 2003)	$m = \frac{G_0 D^2}{16}\theta\left(\pi - \frac{G_0}{6 s_u}\theta\right)$ (Tott-Buswell and Prendergast 2022)

Note: Where r_m = an empirical radius introduced by Cooke (1974) and Randolph and Wroth (1978), s_u = the soil undrained shear strength, b = a soil nonlinearity exponent, γ_{50} = the soil shear strain at a shear stress of 50% of s_u, G_0 = the soil shear modulus at low strain, and B (x, y) = the incomplete Beta function (Olver et al. 2010).

Appendix II. Derivation of General Shear Stress Functions in Eq. (9)

Assuming the variation of normal stresses (and displacements) with depth are negligible, the vertical equilibrium of the soil element in cylindrical coordinates (Fig. 1) yields Eq. (8).

By introducing separation of variables, these two shear stresses can be written as

$$\tau_{rz}(r,\varphi) = R_r(r)\Phi_r(\varphi) \tag{36a}$$

$$\tau_{\varphi z}(r,\varphi) = R_\varphi(r)\Phi_\varphi(\varphi) \tag{36b}$$

where R and Φ = functions of r and φ, respectively. Substituting these functions into Eq. (8) yields

$$r(R_r'\Phi_r) + (R_r\Phi_r) + (R_\varphi\Phi_\varphi') = 0 \tag{37a}$$

$$\frac{rR_r' + R_r}{R_\varphi} = -\frac{\Phi_\Phi'}{\Phi_r} = -a_{r\varphi} \tag{37b}$$

where $a_{r\varphi}$ = positive constant, true for all r and φ values. Taking each side of the equation separately, a pair of ordinary differential equations (ODE) is formed

$$rR_r' + R_r + a_{r\varphi}R_\varphi = 0 \tag{38a}$$

$$\Phi_\varphi' - a_{r\varphi}\Phi_r = 0 \tag{38b}$$

Due to the symmetry of the problem, Φ_r and Φ_φ should be even and odd periodic functions of φ, respectively. Therefore, a natural choice for these functions is sums of sinusoidal and cosinusoidal terms which can form an infinite orthogonal basis for a function space. Considering the general term per function, one obtains

$$\Phi_\varphi = \sin(k\varphi) \tag{39a}$$

$$\Phi_r = \cos(k\varphi) \tag{39b}$$

where k = harmonic integer parameter. Substituting these functions into Eq. (38*b*) and solving yields:

$$a_{r\varphi} = k \tag{40}$$

Inspired by the solution of the elastic problem, it can be assumed, as a first approximation, that R_r is a power-law function of the radial coordinate

$$R_r = C_k r^{n_r} \tag{41}$$

where C_k = integration constant to be determined from the boundary conditions; and n_r = unknown power. This can be substituted into Eq. (38*a*) and solved for R_φ to give

$$R_\varphi = -C_k\left(\frac{n_r+1}{a_{r\varphi}}\right)r^{n_r} \tag{42}$$

Note that a comparison between these two equations show that R_r and R_φ differ only by the proportionality constant $(n_r+1)/a_{r\varphi}$. Thus, their ratio is independent of the radial coordinate.

In addition, a relationship between n_r and k can be established by considering the six compatibility equations between strains, which are necessary to consider as the analysis at hand begins with stresses and establishes displacements by integration of the corresponding strains. These are expressed in radial coordinates below (Carlucci et al. 2013). Since all normal strains are equal to zero ($\varepsilon_{rr} = \varepsilon_{zz} = \varepsilon_{\varphi\varphi} = 0$), the conjugate shear strain $\gamma_{r\varphi}$ is zero, and the rate of change of strains with depth is also zero ($\partial\gamma_{rz}/\partial z = \partial\gamma_{\varphi z}/\partial z = 0$), this leaves two compatibility equations to satisfy

$$-\frac{1}{r}\left(\frac{\partial\gamma_{\varphi z}}{\partial r}\right) + \frac{\partial}{\partial r}\left[\frac{1}{r}\left(\frac{\partial\gamma_{rz}}{\partial\varphi}\right) - \left(\frac{\partial\gamma_{\varphi z}}{\partial r}\right)\right] + \frac{1}{r^2}\gamma_{\varphi z} = 0 \tag{43a}$$

$$\frac{1}{r}\frac{\partial}{\partial\varphi}\left[\frac{\partial\gamma_{\varphi z}}{\partial r} - \frac{1}{r}\left(\frac{\partial\gamma_{rz}}{\partial\varphi}\right)\right] + \frac{1}{r^2}\left(\frac{\partial\gamma_{\varphi z}}{\partial\varphi}\right) = 0 \tag{43b}$$

where $\gamma_{\varphi z} = \tau_{\varphi z}/G$, $\gamma_{rz} = \tau_{rz}/G$; and G = shear modulus which is assumed to be the same for both $\gamma_{\varphi z}$ and γ_{rz}. A less restrictive assumption would be to assume that the shear stiffnesses in the two directions differ by a proportionality constant (i.e., $\tau_{\varphi z}/\gamma_{\varphi z} = s\,\tau_{rz}/\gamma_{rz}$) which is not a function of r or φ, so it can be interpreted as an anisotropy parameter. Such analysis lies beyond the scope of this study.

The shear stresses in the form of Eqs. (36*a*) and (36*b*) [with Eqs. (39*a*), (39*b*), (41), and (42) substituted in] can be converted into their respective shear strains. Substituting these functions of shear strains into both Eqs. (43*a*) and (43*b*) proves that the power-law functions in Eqs. (41) and (42) satisfy the compatibility equations and yields an identical relationship between n_r and k shown in Eq. (44)

$$k^2 = (n_r+1)^2 \tag{44}$$

Considering k to be a positive variable and noting that n_r should be negative (so that stresses and strains attenuate with radial distance from the pile) and on taking square roots, a negative sign is retained

$$n_r = -(k+1) \tag{45}$$

Therefore, taking the shear stresses in the form of Eqs. (36*a*) and (36*b*) and substituting them in Eqs. (39*a*), (39*b*), (41), (42), and (45), the shear stresses in the soil can be written as

$$\tau_{rz} = \tau_{\text{ref}}\sum_{k=1,3,5,7\ldots}^{\infty} C_k\left(\frac{2r}{D}\right)^{-(k+1)}\cos(k\varphi) \tag{46a}$$

$$\tau_{\varphi z} = \tau_{\text{ref}}\sum_{k=1,3,5,7\ldots}^{\infty} C_k\left(\frac{2r}{D}\right)^{-(k+1)}\sin(k\varphi) \tag{46b}$$

where τ_{ref} = arbitrary reference stress. These equations are valid for any odd integer value of k, with an independent C_k value for each term in the summation.

For convenience, an auxiliary parameter $j = (k+1)/2$ is defined, where j is a harmonic parameter of any positive integer value. This yields the shear stresses in the form given also in Eq. (9)

$$\tau_{rz}(r,\varphi) = \tau_{\text{ref}}\sum_{j=1,2,3\ldots}^{\infty} C_j\left(\frac{2r}{D}\right)^{-2j}\cos((2j-1)\varphi) \tag{47a}$$

$$\tau_{\varphi z}(r,\varphi) = \tau_{\text{ref}}\sum_{j=1,2,3\ldots}^{\infty} C_j\left(\frac{2r}{D}\right)^{-2j}\sin((2j-1)\varphi) \tag{47b}$$

Appendix III. Calculation of Fourier Coefficients C_j in the General Solution Neglecting Soil Yield

For each assumed value of φ_s, a system of equations can be developed to obtain a vector $\boldsymbol{C}$ containing unknown coefficients C_j for each value of j

$$\boldsymbol{FC} = \boldsymbol{V} = \begin{bmatrix} f(1,1) & \cdots & f(1,j) & \cdots & f(1,N) \\ \vdots & \ddots & \vdots & \ddots & \vdots \\ f(i,1) & \cdots & f(i,j) & \cdots & f(i,N) \\ \vdots & \ddots & \vdots & \ddots & \vdots \\ f(N,1) & \cdots & f(N,j) & \cdots & f(N,N) \end{bmatrix} \begin{bmatrix} C_1 \\ \vdots \\ C_i \\ \vdots \\ C_N \end{bmatrix} \quad (48)$$

where $\boldsymbol{F} = N \times N$ matrix of components relating to i sums of j products of C_j terms; and $\boldsymbol{V}$ = vector of known values these sums equal. The matrix element $f(i,j)$ corresponds to the contribution of the jth Fourier term to the shear stress at the ith discretization point ($\varphi = \varphi_i$).

Starting with the bonded region [$\varphi_i > \varphi_s$; arc PB on Fig. 4(a)], the soil and pile displacements on the pile periphery can be equated. These can be given by: (1) the geometry of the rotation of a rigid pile cross section [Eq. (2)—with θ given by Eq. (21)] and (2) the soil displacements [Eq. (20)]. This yields the infinite set of linear equations in terms of the unknowns C_j

$$\sum_{j=1,2,3\ldots}^{\infty} C_j f_b(i,j) = \sum_{j=1,2,3\ldots}^{\infty} \frac{C_j}{2j-1}\left[\cos((2j-1)\varphi_i) - \frac{\cos\varphi_i}{\cos\varphi_s}\cos((2j-1)\varphi_s)\right] = 0 \quad (49)$$

where $f_b(i,j)$ = dimensionless component of matrix $\boldsymbol{F}$ [Eq. (48)] when φ_i is in the bonded region. It should be noted that as φ_i tends toward φ_s, then f_b tends toward zero, suggesting that the angle $\varphi_i = \varphi_s$ should not be used as part of a linear system of equations to determine the Fourier coefficients, C_j.

Continuing with the slipped region [$\varphi_i < \varphi_s$; arc CP on Fig. 4(a)], the contact shear stresses at the pile/soil interface in Eq. (9) are equal to the interface strength (i.e., $\tau_{rz} = \alpha s_u$). This yields the infinite set of linear equations in terms of the unknown C_j

$$\sum_{j=1,2,3\ldots}^{\infty} C_j f_s(i,j) = \sum_{j=1,2,3\ldots}^{\infty} C_j \cos((2j-1)\varphi_i) = \alpha \quad (50)$$

where $f_s(i,j)$ = component of matrix $\boldsymbol{F}$ [Eq. (48)] when φ_i is in the slipped region.

Substituting Eqs. (49) and (50) into the matrix in Eq. (48) gives

$$\begin{bmatrix} f_s(1,1) & \ldots & f_s(1,j) & \ldots & f_s(1,N) \\ \vdots & \ddots & \vdots & \ddots & \vdots \\ f_s(i_s,1) & \ldots & f_s(i_s,j) & \ldots & f_s(i_s,N) \\ f_b(i_s+1,1) & \ldots & f_b(i_s+1,j) & \ldots & f_b(i_s+1,N) \\ \vdots & \ddots & \vdots & \ddots & \vdots \\ f_b(N,1) & \ldots & f_b(N,j) & \ldots & f_b(N,N) \end{bmatrix} \begin{bmatrix} C_1 \\ \vdots \\ C_{i_s} \\ C_{i_s+1} \\ \vdots \\ C_N \end{bmatrix} = \begin{bmatrix} \alpha \\ \vdots \\ \alpha \\ 0 \\ \vdots \\ 0 \end{bmatrix} \quad (51)$$

where i_s = index of the largest φ_i within the slipped region. Note this is also the number of discretization points within the slipped region.

Appendix IV. Calculation of Fourier Coefficients C_j in the General Solution Incorporating Soil Yield

Within the yielded region ($\varphi_s < \varphi < \varphi_y$) it is known that $\tau_{\text{mag}} = s_u$ and thus, $\partial\tau_{\text{mag}}/\partial\varphi = 0$ since τ_{mag} is constant. The latter constraint can be expressed by

$$\frac{d\tau_{\text{mag}}}{d\varphi} = 2s_u \frac{X}{2\sqrt{[\sum_{j=1,2,3\ldots}^{\infty} C_j\cos((2j-1)\varphi_i)]^2 + [\sum_{j=1,2,3\ldots}^{\infty} C_j\sin((2j-1)\varphi_i)]^2}} = 0 \quad (52a)$$

$$X = \left[\sum_{j=1,2,3\ldots}^{\infty} (1-2j)C_j\sin((2j-1)\varphi_i)\right]\left[\sum_{j=1,2,3\ldots}^{\infty} C_j\cos((2j-1)\varphi_i)\right] + \left[\sum_{j=1,2,3\ldots}^{\infty} (2j-1)C_j\cos((2j-1)\varphi_i)\right]\left[\sum_{j=1,2,3\ldots}^{\infty} C_j\sin((2j-1)\varphi_i)\right] \quad (52b)$$

τ_{rz} and $\tau_{\varphi z}$ from Eq. (9) can be substituted into X in place of the relevant summations. Thus, given that the square root in the denominator is always nonzero, one obtains

$$\sum_{j=1,2,3\ldots}^{\infty} C_j f_y(i,j) = \sum_{j=1,2,3\ldots}^{\infty} C_j(2j-1)\left[\left(\frac{\tau_{\varphi z}}{\tau_{rz}}\right)\cos((2j-1)\varphi_i) - \sin((2j-1)\varphi_i)\right] = 0 \quad (53)$$

where $f_y(i,j)$ = dimensionless component of matrix $\boldsymbol{F}$ [Eq. (48)] when φ_i is in the yielded region.

This equation is expressed in terms of the stress ratio $\tau_{rz}/\tau_{\varphi z}$, making it a nonlinear function of C_j, which is not compatible with the formation of linear equations required for Eq. (48). However, if the arc step $\delta\varphi$ of the analysis in Fig. 4(a) is small, the ratio $\tau_{\varphi z}/\tau_{rz}$ does not vary significantly between two successive analysis steps and can be taken as equal to the value at the same φ_i during the previous analysis step. In light of this approximation, the presented equation becomes linear in C_j and can be used in Eq. (48) for the zone $\varphi_s < \varphi < \varphi_y$, in which the soil has yielded along the periphery of the pile. Therefore, from Eqs. (49), (50), and (53), a set of simultaneous equations can be set up for each value of i and j assuming a specific φ_y and φ_s

$$\begin{bmatrix} f_s(1,1) & \dots & f_s(1,j) & \dots & f_s(1,N) \\ \vdots & \ddots & \vdots & \ddots & \vdots \\ f_s(i_s,1) & \dots & f_s(i_s,j) & \dots & f_s(i_s,N) \\ f_y(i_s+1,1) & \dots & f_y(i_s+1,j) & \dots & f_y(i_s+1,N) \\ \vdots & \ddots & \vdots & \ddots & \vdots \\ f_y(i_y,1) & \dots & f_y(i_y,j) & \dots & f_y(i_y,N) \\ f_b(i_y+1,1) & \dots & f_b(i_y+1,j) & \dots & f_b(i_y+1,N) \\ \vdots & \ddots & \vdots & \ddots & \vdots \\ f_b(N,1) & \dots & f_b(N,j) & \dots & f_b(N,N) \end{bmatrix} \begin{bmatrix} C_1 \\ \vdots \\ C_{i_s} \\ C_{i_s+1} \\ \vdots \\ C_{i_y} \\ C_{i_y+1} \\ \vdots \\ C_N \end{bmatrix} = \begin{bmatrix} \alpha \\ \vdots \\ \alpha \\ 0 \\ \vdots \\ 0 \\ 0 \\ \vdots \\ 0 \end{bmatrix} \tag{54}$$

where i_y = index of the largest φ_i within the yielded region.

Data Availability Statement

All data, models, and code generated or used during the study appear in the published article.

Acknowledgments

The first author would like to thank the Engineering and Physical Sciences Research Council for their support (Grant No. EP/T517872/1).

Notation

The following symbols are used in this paper:

$a_{r\varphi}$ = positive constant, true for all r and φ values [given by Eq. (40)];
b = soil nonlinearity exponent;
$\boldsymbol{C}$ = vector containing C_j values for specific values of j;
C_j = dimensionless constant determined for each j from boundary conditions;
C_k = dimensionless constant determined for each k from boundary conditions;
D = pile diameter;
$\boldsymbol{F}$ = $N \times N$ matrix of components relating to i sums of j products of C_j terms [Eq. (48)];
$f(i,j)$ = general component of matrix $\mathbf{F}$ [Eq. (48)];
$f_b(i,j)$ = component of matrix $\mathbf{F}$ [Eq. (48)] when φ_i is in the bonded region [Eq. (49)];
$f_s(i,j)$ = component of matrix $\mathbf{F}$ [Eq. (48)] when φ_i is in the slipped region [Eq. (50)];
$f_y(i,j)$ = component of matrix $\mathbf{F}$ [Eq. (48)] when φ_i is in the yielded region [Eq. (53)];
G = shear modulus of the soil;
G_0 = initial shear modulus of the soil;
i = circumference discretization index;
i_s = index of the largest φ_i within the slipped region;
i_y = index of the largest φ_i within the yielded region;
j = positive integer harmonic parameter;
k = positive odd integer valued harmonic parameter;
k_m = linear stiffness of an m-θ curve;
k_v = linear stiffness of a t-z curve;
L = pile length;
m = distributed moment resistance;
m_u = ultimate distributed moment resistance;
N = number of discretization points in the general solution;
n_r = power exponent [given by Eq. (45)];
R = denotes a function of r;
r = radial distance from the center of the pile slice;
r_m = empirical radius;
s_u = soil undrained shear strength;
$u_0(\varphi)$ = vertical soil displacement at the pile/soil interface;
$u_{0p}(\varphi)$ = vertical pile displacements at the pile circumference;
$\boldsymbol{V}$ = vector of values denoting the solutions to $f(i,j)$ [Eq. (48)];
V_b = component of vector $\boldsymbol{V}$ when φ_i is in the bonded region [Eq. (49)];
V_s = component of vector $\boldsymbol{V}$ when φ_i is in the slipped region [Eq. (50)];
V_y = component of vector $\boldsymbol{V}$ when φ_i is in the yielded region [Eq. (51)];
X = parameter given by Eq. (52a);
z = depth measured from the ground surface;
α = empirical adhesion factor;
γ_{rz}, $\gamma_{\varphi z}$, $\gamma_{r\varphi}$ = soil shear strains;
γ_{50} = shear strain when the shear stress is at 50% of s_u;
$\delta\varphi$ = angle in radians between each discretization point;
ε_{rr}, ε_{zz}, $\varepsilon_{\varphi\varphi}$ = normal strains in cylindrical coordinates;
θ = angle of pile slice rotation in radians;

θ_s = slice rotation at which slip at the pile/soil interface ($\tau_{rz,0,C} = \alpha_{su}$) first occurs;
θ_u = slice rotation at which soil yielding ($\tau_{\text{mag}} = s_u$) first occurs;
$\tau_{\text{mag}}(r, \varphi)$ = magnitude of the shear stresses $\left(\tau_{\text{mag}} = \sqrt{\tau_{rz}^2 + \tau_{\varphi z}^2}\right)$;
$\tau_{\text{mag},0}(\varphi)$ = magnitude of the shear stresses at the pile periphery;
τ_{ref} = arbitrary reference shear stress;
$\tau_{rz}(r, \varphi)$ = vertical contact shear stresses;
$\tau_{rz,0}(\varphi)$ = vertical contact shear stresses at the pile periphery;
$\tau_{rz,0,C}$ = maximum value of $\tau_{rz,0}$ at $\varphi = 0$;
$\tau_{r\varphi}$ = horizontal soil shear stress between each horizontal soil slice (assumed to be zero);
$\tau_{\varphi z}(r, \varphi)$ = vertical tangential shear stresses;
$\tau_{\varphi z,0}(\varphi)$ = vertical tangential shear stresses at the pile periphery;
Φ = denotes a function of φ;
φ = aperture angle around the pile periphery, measured from the location of maximum displacement;
φ_i = aperture angle to an arbitrary discretization point, illustrated in Fig. 4(a);
φ_s = largest aperture angle at which slip occurs ($\tau_{rz,0} = \alpha s_u$), illustrated in Fig. 7(a);
$\varphi_{s,u}$ = maximum value of φ_s in the general solution considering soil yield; and
φ_y = largest aperture angle at which soil yield occurs ($\tau_{\text{mag}} = s_u$), illustrated in Fig. 4(b).

Supplemental Materials

An example Python implementation of the general solution is available online in the ASCE library (www.ascelibrary.org).

References

Agapaki, E., X. Karatzia, and G. Mylonakis. 2018. "Higher-order Winkler solutions for laterally loaded piles." In *Proc., 16th European Conf. on Earthquake Engineering*, 1–14. Istanbul, Turkey: European Association for Earthquake Engineering.

ANSI and API (American National Standards Institute and American Petroleum Institute). 2011. *Geotechnical and foundation design considerations*. ANSI/API Recommended Practice 2GEO. Washington, DC: ANSI and API.

Basu, D., and R. Salgado. 2008. "Analysis of laterally loaded piles with rectangular cross sections embedded in layered soil." *Int. J. Numer. Anal. Methods Geomech.* 32 (7): 721–744. https://doi.org/10.1002/nag.639.

Basu, D., R. Salgado, and M. Prezzi. 2009. "A continuum-based model for analysis of laterally loaded piles in layered soils." *Géotechnique* 59 (2): 127–140. https://doi.org/10.1680/geot.2007.00011.

Bateman, A. H. 2025. "Simplified solutions for the non-linear response of axially and laterally loaded piles in clay." Ph.D. thesis, Dept. of Civil Engineering, Univ. of Bristol.

Bateman, A. H., J. J. Crispin, and G. Mylonakis. 2022a. "A simplified analytical model for developing '*t-z*' curves for axially loaded piles." In *Proc., 20th Int. Conf. on Soil Mechanics and Geotechnical Engineering*, 3211–3216. Sydney, NSW, Australia: Australian Geomechanics Society.

Bateman, A. H., J. J. Crispin, P. J. Vardanega, and G. E. Mylonakis. 2022b. "Theoretical *t-z* curves for axially loaded piles." *J. Geotech. Geoenviron. Eng.* 148 (7): 04022052. https://doi.org/10.1061/(ASCE)GT.1943-5606.0002753.

Bateman, A. H., G. Mylonakis, J. Creasey, A. El Hajjar, D. White, B. Cerfontaine, S. Gourvenec, and A. Diambra. 2023a. "*p-y* curves from in-situ ROBOCONE tests: A similarity approach for laterally loaded piles in clay." In *Proc., Symp. on Energy Geotechnics*. Delft, Netherlands: TU Delft OPEN.

Bateman, A. H., G. Mylonakis, and J. J. Crispin. 2023b. "Simplified analytical '*m-θ*' curves for predicting nonlinear lateral pile response." In *Proc., 9th Int. Offshore Site Investigation and Geotechnics Conf.*, 618–625. London: Society for Underwater Technology. https://doi.org/10.3723/SSVU3562.

Byrne, B. W., et al. 2017. "PISA: New design methods for offshore wind turbine monopiles." In *Proc., Offshore Site Investigation and Geotechnics*, 142–161. London: Society for Underwater Technology.

Byrne, B. W., et al. 2020. "PISA design model for monopiles for offshore wind turbines: Application to a stiff glacial clay till." *Géotechnique* 70 (11): 1030–1047. https://doi.org/10.1680/jgeot.18.P.255.

Carlucci, D., N. Payne, and I. Mehmedagic. 2013. *Small strain compatibility conditions of an elastic solid in cylindrical coordinates*. Technical Rep. ARDSM-TR-12001. Wharton, NJ: US Army Armament Research, Development and Engineering Center.

Cooke, R. W. 1974. "The settlement of friction pile foundations." In *Proc., Conf. on Tall Buildings*, 7–19. Selangor, Malaysia: Institution of Engineers.

Creasey, J., et al. 2024. "Initial design and testing of a new site investigation tool for the direct determination of p-y soil reaction curves: ROBOCONE." In *Proc., 18th European Conf. on Soil Mechanics and Geotechnical Engineering*. London: Taylor and Francis.

Davies, R. O., and A. P. S. Selvadurai. 1996. *Elasticity and geomechanics*. Cambridge, UK: Cambridge University Press.

Favaretti, C., A. Lemnitzer, A. W. Stuedlein, and J. Turner. 2015. "Recent discussions of *p-y* formulations for lateral load transfer of deep foundations based on experimental studies." In *Proc., Int. Foundations Congress and Equipment Exposition (IFCEE)*, 388–399. Reston, VA: ASCE. https://doi.org/10.1061/9780784479087.039.

Franke, K. W., and K. M. Rollins. 2013. "Simplified hybrid *p-y* spring model for liquefied soils." *J. Geotech. Geoenviron. Eng.* 139 (4): 564–576. https://doi.org/10.1061/(ASCE)GT.1943-5606.0000750.

Fu, D., Y. Zhang, K. K. Aamodt, and Y. Yan. 2020. "A multi-spring model for monopile analysis in soft clays." *Mar. Struct.* 72 (Jul): 102768. https://doi.org/10.1016/j.marstruc.2020.102768.

Gerolymos, N., and G. Gazetas. 2006. "Development of Winkler model for static and dynamic response of caisson foundations with soil and interface nonlinearities." *Soil Dyn. Earthquake Eng.* 26 (5): 363–376. https://doi.org/10.1016/j.soildyn.2005.12.002.

Guo, W. D. 2012. *Theory and practice of pile foundations*. Boca Raton, FL: CRC Press.

Han, F., M. Prezzi, and R. Salgado. 2017. "Energy-based solutions for non-displacement piles subjected to lateral loads." *Int. J. Geomech.* 17 (11): 04017104. https://doi.org/10.1061/(ASCE)GM.1943-5622.0001012.

Hetenyi, M. 1946. *Beams on elastic foundation*. Ann Arbor, MI: Univ. of Michigan Press.

Hu, Q., F. Han, M. Prezzi, R. Salgado, and M. Zhao. 2022. "Finite-element analysis of the lateral load response of monopiles in layered sand." *J. Geotech. Geoenviron. Eng.* 148 (4): 04022001. https://doi.org/10.1061/(ASCE)GT.1943-5606.0002745.

Jeanjean, P., and A. Zakeri. 2023. "Efficiencies and challenges in offshore wind foundation design." In *Proc., 9th Int. Offshore Site Investigation and Geotechnics Conf.*, 700–728. London: Society for Underwater Technology. https://doi.org/10.3723/CNIE2258.

Jeanjean, P., Y. Zhang, A. Zakeri, K. H. Andersen, R. Gilbert, and A. I. M. J. Senanayake. 2017. "A framework for monotonic *p-y* curves in clays." In *Proc., Offshore Site Investigation Geotechnics 8th Int. Conf. Proc.*, 108–141. London: Society for Underwater Technology. https://doi.org/10.3723/OSIG17.108.

Juirnarongrit, T., and S. A. Ashford. 2006. "Soil-pile response to blast-induced lateral spreading. II: Analysis and Assessment of the *p–y* method." *J. Geotech. Geoenviron. Eng.* 132 (2): 163–172. https://doi.org/10.1061/(ASCE)1090-0241(2006)132:2(163).

Kagawa, T., and L. M. Kraft Jr. 1981. "Dynamic characteristics of lateral load-deflection relationships of flexible piles." *Earthquake Eng. Struct. Dyn.* 9 (1): 53–68. https://doi.org/10.1002/eqe.4290090105.
Kaynia, A. M. 2021. *Analysis of pile foundations subject to static and dynamic loading*. London: CRC Press. https://doi.org/10.1201/9780429354281.
Khalili-Tehrani, P., E. R. Ahlberg, C. Rha, A. Lemnitzer, J. P. Stewart, E. Taciroglu, and J. W. Wallace. 2014. "Nonlinear load-deflection behavior of reinforced concrete drilled piles in stiff clay." *J. Geotech. Geoenviron. Eng.* 140 (3): 04013022. https://doi.org/10.1061/(ASCE)GT.1943-5606.0000957.
Kraft, L. M., R. P. Ray, and T. Kagawa. 1981. "Theoretical *t-z* curves." *J. Geotech. Eng. Div.* 107 (11): 1543–1561. https://doi.org/10.1061/AJGEB6.0001207.
Lai, Y., L. Wang, Y. Zhang, and Y. Hong. 2021. "Site-specific soil reaction model for monopiles in soft clay based on laboratory element stress-strain curves." *Ocean Eng.* 220 (Jan): 108437. https://doi.org/10.1016/j.oceaneng.2020.108437.
Lam, I. P. 2013. "Diameter effects on p-y curves." In *Deep marine foundations—A perspective on the design and construction of deep marine foundations*, edited by R. B. Bittner and R. A. Ellman. Hawthorne, NJ: Deep Foundation Institute.
Lam, I. P., and G. R. Martin. 1986. *Seismic design of highway bridge foundations. Volume 2: Design procedures and guidelines*. Washington, DC: US DOT, Federal Highway Administration.
Matlock, H. 1970. "Correlations for design of laterally loaded piles in soft clay." In *Proc., 2nd Offshore Technology Conf.*, 557–588. Houston: Offshore Technology Conference. https://doi.org/10.4043/1204-MS.
McClelland, B., and J. A. Focht Jr. 1956. "Soil modulus for laterally loaded piles." *J. Soil Mech. Found. Div.* 82 (4): 1081. https://doi.org/10.1061/JSFEAQ.0000023.
Murphy, G., D. Igoe, P. Doherty, and K. Gavin. 2018. "3D FEM approach for laterally loaded monopile design." *Comput. Geotech.* 100 (Aug): 76–83. https://doi.org/10.1016/j.compgeo.2018.03.013.
Mylonakis, G. 2000. "'A new analytical model for settlement analysis of a single pile in multi-layered soil', Discussion to Paper by K.M. Lee and Z.R. Xiao." *Soils Found.* 40 (4): 163–166.
Mylonakis, G. 2001. "Winkler modulus for axially loaded piles." *Géotechnique* 51 (5): 455–461. https://doi.org/10.1680/geot.2001.51.5.455.
Mylonakis, G., and J. J. Crispin. 2021. "Simplified models for lateral static and dynamic analysis of pile foundations." In *Analysis of pile foundations subject to static and dynamic loading*, edited by A. M. Kaynia, 185–245. London: CRC Press. https://doi.org/10.1201/9780429354281-6.
Novak, M., and M. Sheta. 1980. "Approximate approach to contact effects of piles." In *Dynamic response of pile foundations, analytical aspects: Proceedings of a session*, edited by M. W. O'Neill and R. Dobry, 53–79. New York: American Society of Civil Engineers.
Olver, F. W. J., D. W. Lozier, R. F. Boisvert, and C. W. Clark. 2010. *NIST handbook of mathematical functions*. New York: NIST.
Osman, A. S., D. J. White, A. M. Britto, and M. D. Bolton. 2007. "Simple prediction of the undrained displacement of a circular surface foundation on non-linear soil." *Géotechnique* 57 (9): 729–737. https://doi.org/10.1680/geot.2007.57.9.729.
Poulos, H. G. 2017. *Tall building foundation design*. Boca Raton, FL: CRC Press. https://doi.org/10.1201/9781315156071.
Randolph, M. F. 2003. *RATZ Load transfer analysis of axially loaded piles*. Perth, Australia: Centre for Offshore Foundation Systems, Univ. of Western Australia.
Randolph, M. F., and C. P. Wroth. 1978. "Analysis of deformation of vertically loaded piles." *J. Geotech. Eng. Div.* 104 (12): 1465–1488. https://doi.org/10.1061/AJGEB6.0000729.
Reese, L. C., and W. F. Van Impe. 2011. *Single piles and pile grounds under lateral loading*. 2nd ed. Boca Raton, FL: CRC Press.
Salgado, R. 2022. *The engineering of foundations, slopes and retaining structures*. 2nd ed. Boca Raton, FL: CRC Press. https://doi.org/10.1201/b22079.
Sanchez-Salinero, I. 1982. *Static and dynamic stiffness of single piles*. Geotechnical Engineering Rep. No. GR82-31. Austin, TX: Univ. of Texas.
Scott, R. F. 1981. *Foundation analysis*. Englewood Cliffs, NJ: Prentice-Hall.
Skempton, A. W. 1951. "The bearing capacity of clays." In Vol. 1 of *Proc., Building Research Congress*, 180–189. London: Building Research Station.
Skempton, A. W. 1959. "Cast in-situ bored piles in London clay." *Géotechnique* 9 (4): 153–173. https://doi.org/10.1680/geot.1959.9.4.153.
Tott-Buswell, J., and L. J. Prendergast. 2022. "A CPT-based diameter-dependent *m-θ* spring model for lateral pile analysis." In *Proc., Cone Penetration Testing 2022*. Boca Raton, FL: CRC Press. https://doi.org/10.1201/9781003308829-171.
Vardanega, P. J., M. G. Williamson, and M. D. Bolton. 2012. "Bored pile design in stiff clay II: Mechanisms and uncertainty." *Proc. Inst. Civ. Eng. Geotech. Eng.* 165 (4): 233–246. https://doi.org/10.1680/geng.11.00063.
Varun, V., D. Assimaki, and G. Gazetas. 2009. "A simplified model for lateral response of large diameter caisson foundations—Linear elastic formulation." *Soil Dyn. Earthquake Eng.* 29 (2): 268–291. https://doi.org/10.1016/j.soildyn.2008.02.001.
Viggiani, C., A. Mandolini, and G. Russo. 2014. *Piles and pile foundations*. London: CRC Press. https://doi.org/10.1201/b17768.
Vrettos, C. 2021. "Design of piles for static loads." In *Analysis of pile foundations subject to static and dynamic loading*, edited by A. M. Kaynia, 1–51. London: CRC Press. https://doi.org/10.1201/9780429354281-1.
Wan, X., J. P. Doherty, and M. F. Randolph. 2021. "Relationships between lateral and rotational load transfer stiffnesses and soil modulus for the elastic response of monopiles." *Comput. Geotech.* 137 (Sep): 104256. https://doi.org/10.1016/j.compgeo.2021.104256.
Zdravković, L., et al. 2020. "Finite-element modelling of laterally loaded piles in a stiff glacial clay till at Cowden." *Géotechnique* 70 (11): 999–1013. https://doi.org/10.1680/jgeot.18.PISA.005.